Chair of Spacecraft Systems
TUM School of Engineering and Design
Technical University of Munich

Modeling of Attitude Determination and Control Subsystem (ADCS) for a 6U CubeSat for Tracking Objects in Space

Eva Katharina Rieger

Thesis for the attainment of the academic degree

Bachelor of Science (B.Sc.)

at the TUM School of Engineering and Design of the Technical University of Munich.

Examiner:
Prof. Dr. Alessandro Golkar

Supervisor:
M.Sc. Vincenzo Messina

Submitted:
Munich, 02.07.2024

I hereby declare that this thesis is entirely the result of my own work except where otherwise indicated. I have only used the resources given in the list of references.

Munich, 02.07.2024 Eva Katharina Rieger

Zusammenfassung

In dieser Arbeit wurde ein Lagebestimmungs- und Steuerungssystem (ADCS) für einen 6U CubeSat in Python entwickelt und analysiert, insbesondere im Hinblick auf das Enttaumeln des Satellitens und die Ausrichtung des Satellitens auf einen Meteoriden. Es wurden verschiedene Störgrößen implementiert, um durch die Simulation eine möglichst genaue Abbildung der Realität zu erreichen. Dazu gehören Druckmomente der Sonnenstrahlung, Schwerkraftgradienteneffekte, aerodynamische Momente und Momente, die durch das Magnetfeld der Erde verursacht werden. Darüber hinaus wurden die Messwerte der Sensoren mit Rauschen beaufschlagt. Für das Enttaumeln wurden drei Magnetorquers mit zwei Reaktionsrädern und einer proportionalen Regelung kombiniert. Diese Lösung zeigte eine verbesserte Dynamik gegenüber der Konfiguration mit drei Magnetorquern ohne Reaktionsräder, indem das Enttaumeln schneller und effizienter passierte. Im Gegensatz dazu, konnte der vorgeschlagene Lösungsansatz im Fall der Ausrichtung des Satelliten auf einen Meteoriden nicht überzeugen. Hierfür würde eine komplexere Regelung benötigt werden.

Abstract

In this thesis, an attitude determination and control system for a 6U CubeSat was developed and analyzed in Python, particularly concerning the satellite's detumbling and the satellite's alignment with a meteoroid. Various disturbances were implemented in order to achieve the most accurate representation of reality through the simulation. These include solar radiation pressure, gravity gradient effects, aerodynamic torque, and torque caused by the Earth's magnetic field. In addition, the measured values of the sensors were subjected to noise. For detumbling, three magnetorquers were combined with two reaction wheels and proportional control. Compared to the configuration with three magnetorquers and no reaction wheels, these were convincing in that the detumbling was faster and more efficient. In contrast, the proposed solution was not convincing in the case of the satellite's alignment with a meteoroid. This would require a more complex control system.

Contents

List of Figures

List of Tables

Acronyms

ADCS Attitude Determination and Control Subsystem. vii, 1–4, 6–8, 10, 13, 15, 25, 35, 41, 44

CMG control moment gyroscope. 8

ECI Earth-centered inertial. 15, 16, 20, 21, 27

FPCB flexible printed circuit board. 9

NASA National Aeronautics and Space Administration. 3, 11

1 Introduction

1.1 Motivation

Over the last few years CubeSats, standardized small satellites, have become increasingly more significant, since the interest aroused for smaller spacecraft in space missions [20, 6]. CubeSats have revolutionized the space industry by providing a low-cost alternative for space exploration and technology demonstration [26]. As their applications expand, the need for precise attitude determination and control systems (ADCS) becomes critical to mission success.

The ADCS is a crucial component responsible for different tasks that ensure safe operation of the CubeSat. These include maintaining the satellite's orientation and ensuring stability and accurate pointing throughout its missions [14]. Cubesats, in particular, exhibit high angular velocity after launch and orbital insertion. This necessitates a control logic for detumbling [11]. In addition, meteoroids significantly impact satellite operations, as they can damage or destroy satellite components in the event of a collision [1]. Therefore, tracking meteoroids is essential to prevent potential damage and ensure the longevity and safety of satellite missions. Moreover, the interest in tracking meteoroids is also due to scientific purposes, as it can contribute to developments in science.

This thesis aims to improve a simulation model of an Attitude Determination and Control Subsystem ADCS of a 6UCubeSat for space object detection, focusing on optimizing its capability to track objects in space. By developing a complete simulation of various sensors and actuators of the ADCS for a 6U CubeSat in Python, this work seeks to optimize the CubeSat's ability to maintain accurate orientation and tracking capabilities. The primary maneuvers developed and analyzed in this work are detumbling and pointing. This improved ADCS simulation aims to contribute to improved space situational awareness, collision avoidance capabilities and observation of meteoroids. Furthermore, it aims to contribute to the development of more reliable and efficient CubeSat missions, enhancing their ability to operate in increasingly crowded orbital environments.

1.2 Outline of the Thesis

Chapter 2 provides the theoretical background in order for the reader to get an overview of ADCS and CubeSats. In Section 2.1, the fundamentals of CubeSats and CubeSat Missions are discussed, explaining why they have become increasingly significant. The ADCS is then described in detail in Section 2.2, including the different types of sensors, actuators, and the processes of attitude determination and control, along with several control methods. Specific information about the maneuvers detumbling and pointing is provided in Section 2.2.5. Furthermore, the characteristics and impact of meteoroids are explained in Section 2.3.

Chapter 3 introduces the methodology, that is used as well as the implementation in the code. In Section 3.1, the model is explained, including the code, the structure of the ADCS, information on the orbit, the satellite, and configurations. The calculations of the orbit and attitude propagation, disturbances sensors, actuators, and control laws for the maneuvers are discussed in Section 3.4, 3.5, 3.6.1, and 3.6.2.

Chapter 4 presents the results of the simulations. Section 4.1 discusses the behavior of the CubeSat under different conditions, such as ideal conditions, disturbances, and noise. Section 4.2 analyzes the detumbling maneuver and compares different actuator configurations to evaluate their effectiveness. Section 4.3 presents the results of the pointing maneuver and examines the performance of the CubeSat aligning with the target, which is in this case the meteoroid.

Finally, Chapter 5 includes the results and contributions of this work. Section 5.1 summarizes the main results and findings from this thesis. Section 5.2 provides an outlook for future work and suggests possible areas for further research and development in the field of CubeSat missions and ADCS technologies.

2 Theoretical Background

This chapter presents the basics that precede this thesis. Chapter 2.1 introduces the CubeSats on which this work is based. In addition to general data such as dimensions and weight, the advantages and reasons for the usage of CubeSats are provided. Subsequently, state-of-the-art examples of Cubesat applications in the industry are presented. In chapter 2.2, the ADCS applied to the CubeSat is described in detail. The interfaces of the ADCS to the CubeSat as sensors and actuators are presented first, followed by the main components, attitude determination, and attitude control. For the sensors and actuators, a wide variety of different mechanisms and their areas of application are mentioned. The functionality and physical principles of attitude determination algorithms and attitude control are presented including various control strategies. The detumbling maneuver and potential control strategies are then discussed in particular, while an overview of meteoroids and their impact on space missions is provided for the pointing analysis.

2.1 CubeSats

CubeSats are a class of small satellites that adhere to a standardized unit measurement of 10x10x10 centimeters, known as a 1U CubeSat, with a mass of up to 1.33 kg [6]. Over the last decade, there has been a growing interest in smaller spacecraft with compact instrument suites or single sensors from both practical and technical perspectives [20]. The ever increasing interest in CubeSats is due to their cost-effectiveness and versatility, as these small satellites have demonstrated significant scientific capabilities [26].

CubeSats were primarily designed for educational purposes or to demonstrate capabilities, with scientific research being a secondary goal. However, researchers have been pleasantly surprised by the high-quality scientific data that constellations of CubeSats can provide [24]. The main motivation behind designing CubeSats was to offer academia a standardized framework to reduce development costs and time, making space more accessible both financially and in terms of launch availability. Academia was key in designing, constructing, and launching the first CubeSats. Early CubeSats were predominantly 1U in size, reflecting the emphasis on simplicity and cost-effectiveness. As the CubeSat standard gained acceptance and confidence grew, larger configurations like 3U CubeSats, which have a mass range of 4 to 6 kg, became more appealing. Recently, even larger CubeSats, such as 6U and 12U, have become common, catering to the expanding variety of satellite applications, as illustrated in Figure 2.1. [4]

CubeSats are revolutionizing space research by making it accessible to public and private entities. Their small size and compatibility with off-the-shelf parts allow them to be launched cost-effectively, often as secondary payloads alongside larger missions. They can even be deployed from the International Space Station, sometimes up to six at a time. This has significantly reduced satellite development costs and opened opportunities for testing new instruments and creating satellite constellations. [26]

CubeSats' modularity and the extensive use of commercial off-the-shelf subsystems allow for rapid project readiness, typically within one to two years, compared to the traditional satellite schedules [28]. CubeSats can act collectively, collecting simultaneous, multipoint data with identical instruments across extensive regions. This approach is akin to multiple weather sensors aiding in understanding global weather systems, thereby enhancing our comprehension of the space environment. For instance, a new series of CubeSats is currently in orbit, performing various scientific investigations and technology demonstrations, marking the first time National Aeronautics and Space Administration (NASA) has launched CubeSats on a rocket designed specifically for small payloads. This includes the CubeSat Compact Radiation Belt Explorer (CeREs), which measures high-energy particles in Earth's radiation belt. Additionally, NASA has proposed several missions to push CubeSat technology further. One such mission is CUVE, which aims

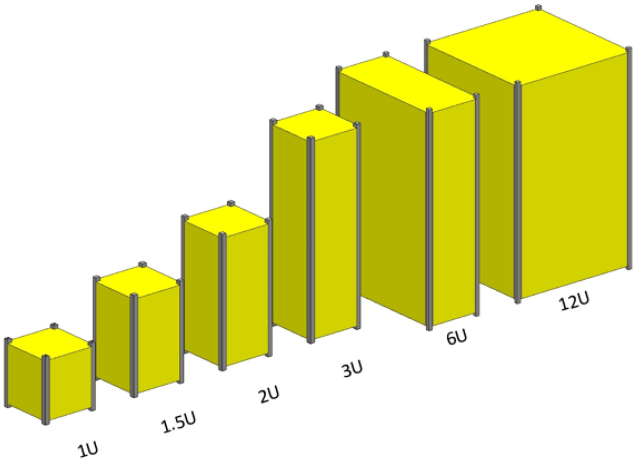

Figure 2.1 CubeSats Sizes from 1U to 12U [6].

to explore Venus's atmosphere using ultraviolet-sensitive instruments and an innovative carbon-nanotube light-gathering mirror. [26]

The European Space Agency is also leveraging CubeSats to augment solar system exploration. For example, the GOMX-4B mission, a 6-Unit CubeSat mission, demonstrated inter-satellite links and propulsion technologies. It carried payloads such as the HyperScout compact hyperspectral imager and a new star tracker. This mission successfully concluded in December 2018, highlighting the growing role of CubeSats in advanced space missions. [28]

2.2 Attitude Determination and Control Systems (ADCS)

The ADCS is a crucial subsystem for stabilizing the spacecraft and orienting it in desired directions throughout the mission, despite external disturbance torques acting on it. The ADCS utilizes sensors to determine the spacecraft's attitude, while actuators are employed to control it. Additionally, the ADCS often closely interacts with other onboard subsystems, particularly propulsion and navigation functions [14].

Figure 2.2 shows a complete diagram of the components of an ADCS acting together.

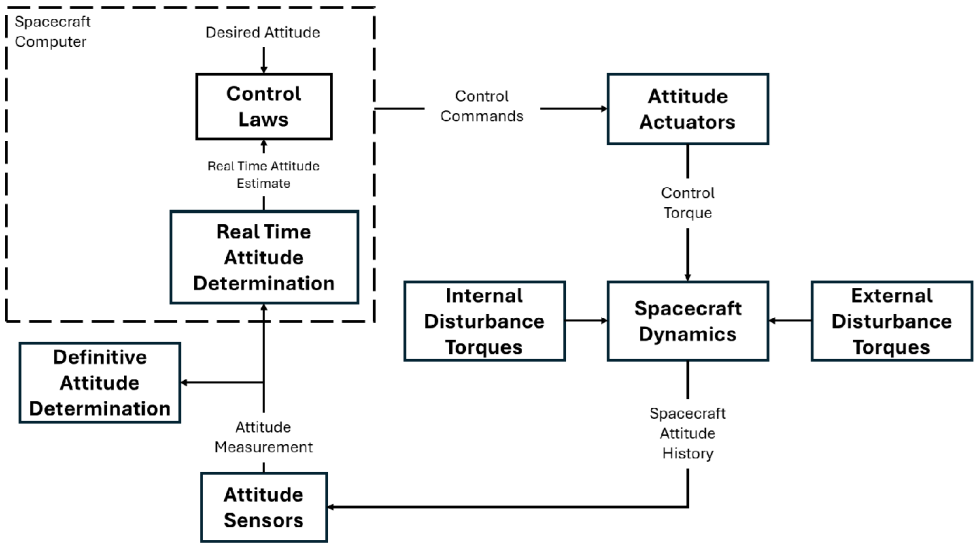

Figure 2.2 Diagram of an Attitude Determination and Control System [14].

As shown in the figure, the spacecraft dynamics are influenced by internal and external disturbance torques, as well as by the control torques provided by the actuators. The attitude sensors measure the attitude, while the spacecraft computer is responsible for estimating the real-time attitude and applying the control laws. The control commands are fed back to the attitude actuators, which generate the required torque for the maneuver.

The attitude adjustment of a spacecraft is described by the Euler equations for rotational dynamics in the spacecraft's reference frame:

$$\dot{\boldsymbol{H}} = \boldsymbol{T} - \boldsymbol{\omega} \times \boldsymbol{H} \tag{2.1}$$

The equation illustrates the conservation of angular momentum $\boldsymbol{H}$. $\boldsymbol{T}$ denotes the applied external torque, whereas the ω represents the angular velocity. It shows that the magnitude of the angular momentum can only be changed by applying external torques. If there are no external torques and one part of a system begins to rotate in one direction, another part must rotate in the opposite direction to maintain the total angular momentum. In addition, the angular velocity ω of a spacecraft can be linked to its angular momentum H by the equation

$$\boldsymbol{H} = \boldsymbol{I}\omega + h. \tag{2.2}$$

Here $\boldsymbol{I}$ represents the moment of inertia and h takes into account the angular momentum stored by components such as reaction wheels or gyroscopes within the spacecraft. This relationship is essential for formulating the Euler equations in matrix form

$$\boldsymbol{I}\dot{\boldsymbol{\omega}} = \boldsymbol{T} - \dot{h} - \dot{\boldsymbol{I}}\omega - \omega \times \boldsymbol{H}, \tag{2.3}$$

which explains the various factors that influence the attitude adjustment of spacecraft [25].

2.2.1 Sensors

Sensors serve various purposes on the spacecraft, from determining the attitude and attitude rates to establishing the relative orientation or positions of spacecraft components [19]. The selection of sensors is

primarily driven by the spacecraft's required orientation and the desired accuracy. Furthermore, considerations such as redundancy, fault tolerance, field of view requirements, and available data rates have to be taken into account for sensor deployment [14]. There are several types of sensors explained in the latter.

Figure 2.3 provides an overview of typical ADCS sensors and their performance range, weight, and power requirements.

Sensor	Typical Performance Range	Wt Range (kg)	Power (W)
Inertial Measurement Unit (Gyros & Accelerometers)	Gyro drift rate = 0.003 deg/hr to 1 deg/hr, accel. Linearity = 1 to 5 x 10^{-6} g/g² over range of 20 to 60 9	1 to 15	10 to 200
Sun Sensors	Accuracy = 0.005 deg to 3 deg	0.1 to 2	0 to 3
Star Sensors (Scanners & Mappers)	Attitude accuracy = 1 arc sec to 1 arc min 0.0003 deg to 0.01 deg	2 to 5	5 to 20
Horizon Sensors • *ScannerlPipper* • *Fixed Head (Static)*	Attitude accuracy: 0.1 deg to 1 deg (LEO) < 0.1 deg to 0.25 deg	 1 to 4 0.5 to 3.5	 5 to 10 0.3 to 5
Magnetometer	Attitude accuracy = 0.5 deg to 3 deg		

Figure 2.3 Table of Typical ADCS Sensors with Significant Data [14].

It is evident that star sensors offer the highest accuracy, while gyroscopes have the highest power consumption [14].

Horizon sensors use infrared technology to measure temperature differences between the cold of deep space and the heat of the Earth's atmosphere, approximately 40 km above the surface. There are narrow field-of-view-fixed-head types for spinning spacecraft, also known as pippers or horizon crossing indicators, measuring Earth phase and chord angles to determine two angles to the Earth vector. Scanning sensors employ rotating mirrors or lenses and are often paired to enhance reliability. The typical accuracy for these sensors ranges from 0.1 degree to 0.25 degrees, with some achieving accuracies as precise as 0.03 degrees [14]. In addition to the simple infrared horizon indicators (HCI), there are more advanced thermopile sensors which are capable of detecting temperature contrasts between the poles and equator. Recent academic attention has focused on horizon sensors for CubeSats, showing promising outcomes [2].

Magnetometers measure the direction and size of the local magnetic field to estimate 2-axis information about the spacecraft's attitude. Although they are simple, reliable, and lightweight, compared to Star or Horizon sensors, the accuracy of the magnetometer is not as good. Therefore, it is often fused with data from Sun or Horizon Sensors to enhance accuracy [2, 14].

Star sensors are the most used for missions requiring high accuracy and have become increasingly important in recent years. Star sensors, including scanners and trackers, are crucial in spacecraft attitude determination. Scanners are employed on spinning spacecraft where the scanner's field of view captures stars that pass through several slits. This allows the vehicle's attitude to be derivated after several crossings [14]. On the other hand, trackers are used on 3-axis stabilized spacecraft to precisely track one or more stars, providing 2- or 3-axis attitude information. Advanced trackers identify bright stars and recognize specific star patterns, aligning their orientation with an onboard star catalog to provide accurate 3-axis attitude several times per second [2, 14]. Star sensors are renowned for their accuracy, although careful consideration is necessary in their specification and deployment. Firstly, a degree of spacecraft stabilization is required before accurate pointing can be achieved. This initial stabilization requires supplementary sensors, which leads to increasing system costs. Moreover, star sensors can be sensitive to

sunlight, moonlight, or planetary interference, which potentially requires specific operational accommodations. Star trackers are often complemented with gyroscopes to counteract limitations during periods of celestial interference, such as from the Sun or Moon. Gyros provide initial stabilization and support continuous operation, while star trackers are responsible for high accuracy. This combination ensures high accuracy and reliability, leveraging gyroscopes for immediate stabilization and star trackers for precise, low-frequency external referencing. [2, 14]

Sun sensors detect visible light and measure the angles between their mounting base and incoming sunlight. Although they require clear fields of view to function effectively, these sensors are reliable and accurate and are often used in attitude determination systems. ADCS with Sun Sensors must be capable of managing the regular loss of data due to eclipse periods, which are very common in low-Earth orbits. Sun sensors can achieve accuracies smaller than 0.01 degrees, although practical limitations such as structural bending on large spacecraft can reduce the accuracy. Spinning satellites use Sun sensors that are specially designed to measure the angle of the Sun with respect to the spin axis of the spacecraft [14]. Furthermore they are also utilized for fault detection and recovery due to the Sun's consistent brightness. There are various types of Sun sensors that operate based on different principles, including cosine detectors, quadrant detectors, digital Sun sensors, and Sun cameras [2].

Gyroscopes, a type of initial sensor, measure a spacecraft's speed or angle of rotation from an initial reference. Often, these are combined with Sun or Star Trackers for more precise attitude control of the satellite as well as for nutation damping or attitude control during the use of thrusters [14].

There are several designs, from simple single-axis devices to 3 orthogonal axes of gyroscopes, such as the Inertial Reference Unit (IRU). In addition, there are also units consisting of 3 orthogonal gyroscopes and 3 orthogonal accelerometers, the Inertial Measurement Unit (IMU). In modern small satellites, mainly fiber optic gyros (FOGs), which are characterized by low cost and excellent performance, and microelectromechanical system (MEMs) gyros are used. Resonator gyros and ring laser gyros are further examples of gyroscope types, whereas these are rarely considered for CubeSat due to their size, weight, performance and price. Various properties, such as bias stability, angle random walk, dynamic range, sample rate, etc influence the performance of gyroscopes. [2]

In recent years, there has been significant interest in advancing the speed of star trackers. In [16] the author explores the potential of high-speed star trackers equipped with modern optics, sensors, and computing systems. The research examines the sensitivity of an optoelectrical acquisition system to faint stars and proposes an algorithm tailored for high-speed operation.

2.2.2 Actuators

Figure 2.4 outlines performance range, weight and power requirements.

Actuator	Typical Performance Range	Weight (kg)	Power (W)
Thrusters			
Hot Gas (Hydrazine)	0.5 to 9,000 N*	Variable†	N/A†
Cold Gas	< 5 N*	Variable†	N/A†
Reaction and Momentum Wheels	0.4 to 400 N·m·s for momentum wheels at 1,200 to 5,000 rpm; max torques from 0.01 to 1 N·m	2 to 20	10 to 110
Control Moment Gyros (CMG)	25 to 500 N·m of torque	>10	90 to 150
Magnetic Torquers	1 to 4,000 A·m^{2}‡	0.4 to 50	0.6 to 16

* Multiply by moment arm (typically 1 to 2 m) to get torque.
† Chap. 17 discusses weight and power for thruster systems in more detail.
‡ For 700-km orbit and maximum Earth field of 0.4 gauss, the maximum torques would be 4.5 x 10^{-5} N·m to 0.18 N·m (see Table 11-9B).

Figure 2.4 Table of Typical ADCS Actuators with Significant Data [14].

Comparing the actuators, thrusters can generate the highest torque, reaching up to $18000Nm$. In contrast, reaction and torque wheels, control moment gyroscope (CMG)s, and magnetic torquers provide torque with varying precision and power consumption [14].

Reaction wheels function as torque motors with high-inertia rotors that can rotate in both directions to control one axis per wheel. Momentum wheels, a type of reaction wheel, maintain a nominal rotational speed above zero and generate a constant angular momentum that provides gyroscopic stiffness along two axes while allowing precise control of motor torque about the third axis [14]. Miniaturized reaction wheels enable 3-axis precision pointing for small spacecraft and must be selected, taking into account parameters such as the mass of the spacecraft and the required rotational performance. Three orthogonally installed wheels are required for full three-axis control, although a four-wheel arrangement is often used for redundancy. Periodic desaturation with external torque actuators, such as thrusters or magnetic torques, is essential. Inclined or angled configurations with multiple wheels provide cross-coupled torques, offering a backup option with reduced performance if one wheel fails [2]. Torque capability and momentum-storage capability are limiting factors of reaction wheels [19].

If higher torques are needed, CMGs are preferred to reaction wheels. These gyros consist of single or double-gimbal-mounted wheels that rotate at a constant speed. By adjusting the gimbal axis, significant torque can be generated that varies with the rotor speed and gimbal rotation rate. CMG systems can provide considerable torque around all three orthogonal axes of a spacecraft, making them suitable for fast and agile maneuvers. However, they require more complicated control laws and momentum exchange for desaturation and are also more costly and heavier. [14]

Thrusters are an alternative to magnetic torques used for attitude control during orbit-change maneuvers or momentum unloading [19]. Hereby torque is produced by ejecting masses. A distinction can be made between hot-gas systems and cold-gas systems. In hot-gas systems, which are either bipropellant or monopropellant, energy is generated by a chemical reaction. Whereas in cold-gas systems, energy is obtained from the latent heat of a phase change or the work of compression without a phase change. The latter is predominantly employed in small satellites [14]. Magnetic Torquers, consisting of magnetic coils or electromagnets, generate magnetic dipole moments to control attitude and angular momentum [19]. They are used to counteract spacecraft's residual magnetic fields or attitude deviation caused by disturbances from the environment [29]. In addition they are capable of desaturating momentum-exchange systems, although the process takes longer than for thrusters. The torque is produced proportional to the Earth's magnetic field, which is fluctuating [14]. An air cole generates a magnetic dipole moment $\mathbf{m}$ described by the equation

$$\mathbf{m} = NIA\mathbf{n}. \tag{2.4}$$

Here, N represents the number of turns of wires, I is the current in the coil, A the area surrounded by the coil and $\mathbf{n}$ denotes a unit vector normal to the coil's plane [19, 29].

The magnetic dipole moment $\vec{m}$ interacts with the Earth's magnetic field, resulting in a torque described by

$$\mathbf{T} = \mathbf{m} \times \mathbf{B}, \tag{2.5}$$

where $\mathbf{B}$ is the Earth's magnetic field [19].

Recent advancements in reaction wheel design for CubeSats, as discussed in [15], emphasize the use of flexible printed circuit board (FPCB) windings and Halbach magnet arrays on reaction wheels to enhance angular momentum control. This innovative approach features a coreless stator with FPCB windings and an outer rotor equipped with a Halbach magnet array to optimize and smooth the torque. This design has a double-layer rotor consisting of an inner and an outer yoke, in contrast to conventional reaction wheels with a single-layer outer rotor. This configuration eliminates the magnetic force on the bearing caused by the interaction between the stator yokes and the magnets. Experimental results indicate that the proposed reaction wheel using FPCB windings performs similarly to conventional reaction wheels with enameled copper windings. However, it eliminates the need for the potting process for windings, which increases overall reliability and is lighter. [15]

Additionally, recent developments in actuator technology for CubeSats have introduced the use of (printed circuit board) PCB-integrated mounted planar coils acting as pseudo-2D magnetorquers to manage high tumbling rates after deployment. As highlighted in [12], these innovations are particularly beneficial for larger CubeSats (2U and 4U). Traditionally, CubeSats utilize magnetorquer rods for initial detumbling and reaction wheels for fine-tuning. The study, however, proposes using embedded planar coils to achieve detumbling without secondary actuators by employing an intelligent projection-based B-Dot control. The performance parameters for different coil combinations are thermally assessed to ensure a stable thermal profile, as the planar coils are embedded within the multilayered PCB as copper traces. Comparing these performance parameters of the proposed coils with those of commercial actuators' revealed that the embedded planar magnetorquers perform better than the commercial alternatives. [12]

The increasing requirements for precise attitude control of spacecraft and greater autonomy necessitate the use of on-board computers (OBCs) or digital processors. These digital systems offer significant advantages, such as the ability to process complex data from different sensors and the flexibility to update control laws through ground commands [29].

2.2.3 Attitude Determination

Attitude determination describes the calculation of the attitude of the spacecraft relative to an inertial system or an object, such as the earth. Attitude can be divided into single-axis attitude and three-axis attitude. Single-axis attitude refers to defining the orientation of a single spacecraft axis within inertial space, typically the spin axis in spin-stabilized spacecraft but adaptable to any axis in spinning or three-axis stabilized spacecraft. To determine single-axis attitude, two independent parameters, such as the right ascension and declination of the spin axis, are required. This single-axis attitude can be represented as a unit vector in inertial space or as a geometric point on the celestial sphere whose center is the spacecraft. The vector representation is preferred for numerical calculations, while the geometric representation is utilized for analytical purposes and physical arguments. By specifying the orientation of a single axis, the overall orientation of the spacecraft is not fully determined, as the rotation around this axis remains undetermined. To fully determine the inertial orientation of a rigid spacecraft, a third independent parameter, such as the azimuth about the spin axis of a point on the spacecraft relative to some object in inertial space, is required. This comprehensive specification, involving three independent components, is commonly known as three-axis attitude, as it fixes the orientation of all three orthogonal spacecraft axes within inertial space. For three-axis stabilized spacecraft, these three parameters are mostly chosen to be the Euler angles, which are three angles and define the spacecraft-fixed coordinates relative to inertial coordinates. [29]

Recent advancements in satellite attitude estimation, as discussed by researchers in [5], highlight the limitations of traditional Kalman filter (KF) methods, which often neglect previous time-step's posteriori

measurement residuals and face challenges with model errors. A novel approach, the robust double gain unscented Kalman filter (RDG-UKF), has been developed to overcome these shortcomings for small satellites. This method involves deriving the second Kalman gain, K2k, to better utilize the previous timestep's measurement residual and thereby improving the efficiency of measurement data usage. In addition, the orthogonal sequence principle and the unscented transform (UT) strategy are implemented to improve the Kalman filter's robustness and performance and mitigate the effects of existing uncertainty model errors. Numerical simulations have shown that RDG-UKF outperforms classical unscented Kalman filters (UKF) in terms of effectiveness and robustness in dealing with model errors and low precision sensors for the attitude estimation of small satellites. [5]

2.2.4 Attitude Control

Attitude Control describes the action of reorienting the spacecraft toward a desired direction [29]. A distinction is made between passive and active attitude control systems. A passive system utilizes the physical properties of the spacecraft and includes a control actuator to provide control. Whereas active control systems can either transfer momentum or utilize external torques produced by thrusters or magnetic torquers [19].

For the ADCS there are various control methods, including for instance Passive Control Techniques, Spin Control Techniques, and Three-axis Control Techniques, each with their typical characteristics [14].

Gravity-gradient control is one example of a Passive Control Technique. It relies on a spacecraft's inertial properties to maintain Earth-pointing orientation. The principle is based on the tendency of an extended object in a gravity field to align its longitudinal axis with the Earth's center. The produced torques decrease with the cube of the orbit radius and are symmetric around the nadir vector, thereby not affecting the yaw around this vector. This method is typically used for simple, near-Earth orbit spacecraft that do not require yaw orientation. Often deployed booms are utilized to achieve the necessary inertias. Additionally, passive control can involve using dampers to minimize small oscillations, known as libration, around the nadir vector due to disturbances. [14]

Spin stabilization is a passive control technique in which the spacecraft rotates and keeps its angular momentum vector relatively stable in inertial space. This method provides gyroscopic stability to resist disturbance torques around two axes and is most stable when spinning about the axis with the largest moment of inertia. The onboard energy dissipation mechanisms will naturally drive the spacecraft toward this stable state. While spin stabilization allows for simple, long-term operation and offers advantages such as a thermally stable environment and sensor scanning capability, it also requires careful control of mass properties for stability. Furthermore, it consumes more fuel for reorientation, making it less suitable for payloads that require frequent reorientation (Spin Control Techniques). [14]

When reorienting a spinning body with angular momentum h, a constant torque T results in an angular velocity ω, which is perpendicular to T and h. The magnitude is given by

$$\omega = \frac{T}{h}. \tag{2.6}$$

The required torque, therefore, increases with the stored momentum. Three-axis control techniques are more prevalent in modern spacecraft compared to spin or gravity gradient stabilization methods. These spacecraft are able to maneuver and achieve stability and accuracy depending on their sensors and actuators, however, they are also characterized by higher cost and complexity. Control torques in three-axis systems are generated by combinations of reaction wheels, control torque gyros, thrusters, or magnetic torques. Typically, these systems use either a momentum bias with a momentum wheel along the pitch axis or a zero momentum, employing a reaction wheel on each axis. Both configurations often require the use of thrusters or magnetic torques in addition to the wheels. [14]

As an illustration of contemporary control algorithms, the authors of [8] introduce a novel simplified intelligent proportional-integral (SI PI) control algorithm for CubeSat ADCS, essential for managing attitude drift in modern small satellite missions. This algorithm operates without traditional controller gains parameters

and employs various sensors, including magnetometers and gyroscopes, to achieve precise attitude adjustments. Validation results demonstrate errors of no more than 0.1 degree, highlighting its effectiveness in ensuring spacecraft stability.

2.2.5 Maneuver

In this section, typical satellite maneuvers such as detumbling and pointing are explained.

Detumbling

Small satellites are often subjected to rapid rotation when they are released from a launch vehicle. This rotation can interfere with the synchronization of the attitude observer with the magnetometer readings. For this reason, simple and reliable control laws that do not require precise attitude information are often used. These mechanisms, known as detumbling mechanisms, help to reduce the satellite's angular momentum. A widely accepted method for demagnetizing very small satellites is B-dot steering. This method uses magnetorquers as actuators and a magnetometer as a sensor. The B-dot control law is based on the time derivative of the measured magnetic field vector, hence the name B-dot. [11]

Pointing and Tracking

As space technology advances, the accumulation of disused and discarded satellites in orbit poses a significant risk to active spacecraft. This situation has led to a pressing need for on-orbit servicing missions, which focus on tasks such as debris removal and conducting space observations. In [30], an approaching and pointing tracking control scheme and a model predictive controller based on a quadratic programming algorithm are proposed.

Another typical maneuver is sun tracking, which involves aligning the satellite's solar panels with the Sun to maximize power generation. This maneuver is essential to ensure the satellite generates sufficient electrical power to efficiently operate its payloads and systems. In the research [21], a sun-tracking law is presented to maximize power generation. It was validated using a realistic mission scenario, showing improved performance compared to other techniques. It was tested in a realistic mission scenario, demonstrating superior performance compared to other methods [21].

Additionally space observation for scientific purposes is also necessary. This includes the tracking of meteoroids, which is a typical maneuver. The next Chapter explains the importance of meteoroids and the necessity of tracking them.

2.3 Meteoroids

A meteoroid is a natural solid object which revolves around the sun or any object in interplanetary space. These objects are smaller than asteroids or comets and range from 30 μm to 1 meter. Smaller particles than meteoroids are classified as micrometeoroids or cosmic dust grains. When a meteoroid successfully passes through the Earth's atmosphere and reaches the surface, it is called a meteorite. [9, 13]

Meteoric phenomena occur when meteoroids enter the Earth's atmosphere. As a meteoroid travels through the atmosphere, it interacts with air molecules, leading to extreme melting and vaporization. The luminosity of the vaporized meteoroid produces the visible phenomenon known as a meteor, commonly referred to as a "shooting star". Additionally, the air is ionized along the meteor's path, creating ion trains that reflect radio waves and can sometimes be seen with the naked eye. Due to vaporization, fusion, and fragmentation, the meteoroid loses mass, referred to as ablation. Furthermore, the resistance of the atmosphere leads to the deceleration of the meteoroid. Ablation depends on the body's angular velocity, while the deceleration depends on its mass. Consequently, both phenomena affect each other. [3]

Established in October 2004, NASA's Meteoroid Environment Office (MEO) is responsible for understanding and minimizing the risks posed by meteoroid impacts on spacecraft in and beyond Earth's orbit.

Meteoroids pose a danger as they can destroy components such as machines and electronics and can also puncture pressurized volumes. Although there is no exact proof that meteoroids have destroyed a spacecraft, several anomalies during the flight have been attributed to meteoroid impacts. For instance, the Olympus satellite was lost due to a control system failure caused by a Perseid meteor shower impact. By understanding the meteoroid environment, spacecraft designers can better protect critical components and avoid crucial operations. [1]

A recent example of meteoroid activity involves the λ-Sculptorid meteor shower, produced by the comet 46P/Wirtanen, predicted for December 12, 2023. Observations were conducted in Australia, New Zealand, and Oceania to determine the size distribution of meteoroids in the shower. 23 λ-Sculptorid orbits were recorded in total. The observed meteoroids had a mean mass of 0.5 grams, with diameters around 10 mm, because of the low in-atmosphere speed of 15 km/s. [27]

3 Methodology

This chapter presents the methodology and the associated equations on which the ADCS implementation is based. First, the simulation model and an overview of the structure of the implementation in this thesis are presented. Then, all subparts are described in detail. First, the implementation of attitude determination is discussed, and then the disturbances, sensors, and actuators are presented. Finally, the control law is outlined. The formulas and derivations presented in this chapter are primarily based on the work [17]. In the equations, vectors are represented by bold lowercase letters, matrices by bold capital letters, and scalars by regular lowercase letters.

3.1 Introduction to the Model

This section introduces the simulation framework developed for the ADCS of a 6UCubeSat to perform maneuvers such as detumbling, pointing, and tracking objects in space.

The ADCS subsystem simulation includes the satellite's spacecraft dynamics, disturbances acting on the satellite, sensors for attitude determination, and actuators and control laws. Version Python 3.12 was used for the modeling. The developed code is available at [22].

Figure 3.1 shows the different blocks of the code and their interactions. The inputs and outputs of each component are also depicted, which illustrates the data flow through the system and how each part contributes to the overall functionality of the ADCS.

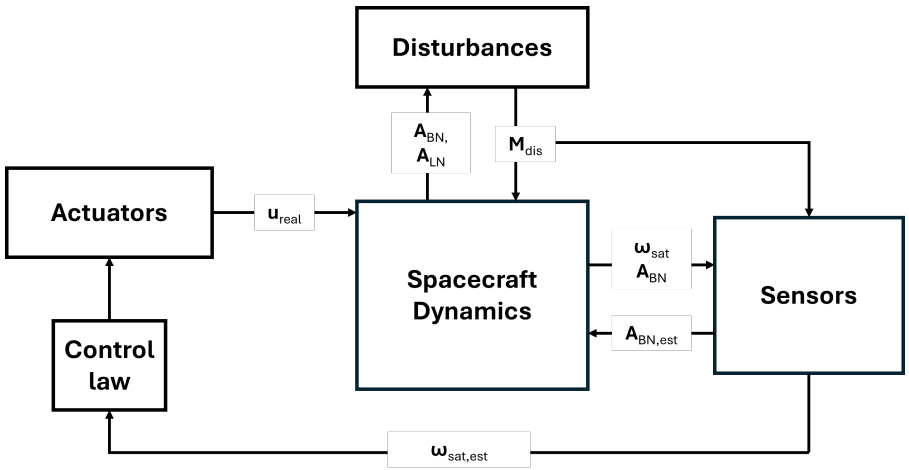

Figure 3.1 Block Diagram of ADCS Simulation Interactions, illustrating the components, their inputs, and outputs.

The spacecraft's dynamics are influenced by the disturbance torques $\mathbf{M}_{dis}$ and control torques $\mathbf{u}_{real}$ generated by the actuators. As output, it delivers the angular velocity $\boldsymbol{\omega}_{sat}$ and rotation matrix from the inertial frame to the body-fixed frame $\mathbf{A}_{BN}$. The sensors provide the estimated attitude $\mathbf{A}_{BN,est}$ and angular velocity $\boldsymbol{\omega}_{sat,est}$.

The CubeSat is assumed to be in a Low-Earth Orbit (LEO), with a semi-major axis of 7070 km, corresponding to an altitude of approximately 700-800 km above the Earth's surface. For the calculations, the Earth's radius R_{Earth} is taken as 6378.137 km, and the Earth's angular velocity ω_E is taken as $\frac{2\pi}{24\times60\times60}$ rad/s, which equals 7.2921159×10^{-5} rad/s.

For the Subsystem a 6U CubeSat configuration was used with the data provided in table 3.1:

Parameter	Value	Unit
Mass	10	kg
Dimensions (L x W x H)	0.2 x 0.3 x 0.1	m
Inertia Matrix I	$\begin{bmatrix} 0.055 & 0 & 0 \\ 0 & 0.0504 & 0 \\ 0 & 0 & 0.0504 \end{bmatrix}$	kg·m²
x_{cm}	0.005234	m
y_{cm}	0.0071282	m
z_{cm}	0.005172	m
Sensor Types	Sun Sensor, Star Sensor, Magnetometer, Gyroscope	
Actuator Types	Reaction Wheels, Magnetorquers	

Table 3.1 CubeSat Configuration Data

The CubeSat has a mass of 10 kg, which is standard for 6U CubeSats, and dimensions of 0.2 x 0.3 x 0.1 meters. In this simulation case, the inertia matrix is assumed and provided as a 3x3 diagonal matrix with I_{xx}, I_{yy}, and I_{zz} components, representing the moments of inertia about the x, y, and z axes, respectively. The 6U configuration considered in this thesis consists of two cubes in a row and three in a column, which explains the given dimensions. The center of mass coordinates are x_{cm}, y_{cm}, z_{cm}.

Various sensors have been used, including three Sun sensors, three Star sensors, one magnetometer, and one gyroscope. Three reaction wheels and three magnetorquers are employed as actuators. The graphical representation of the CubeSat with its sensors and actuators can be seen in Figure 3.2.

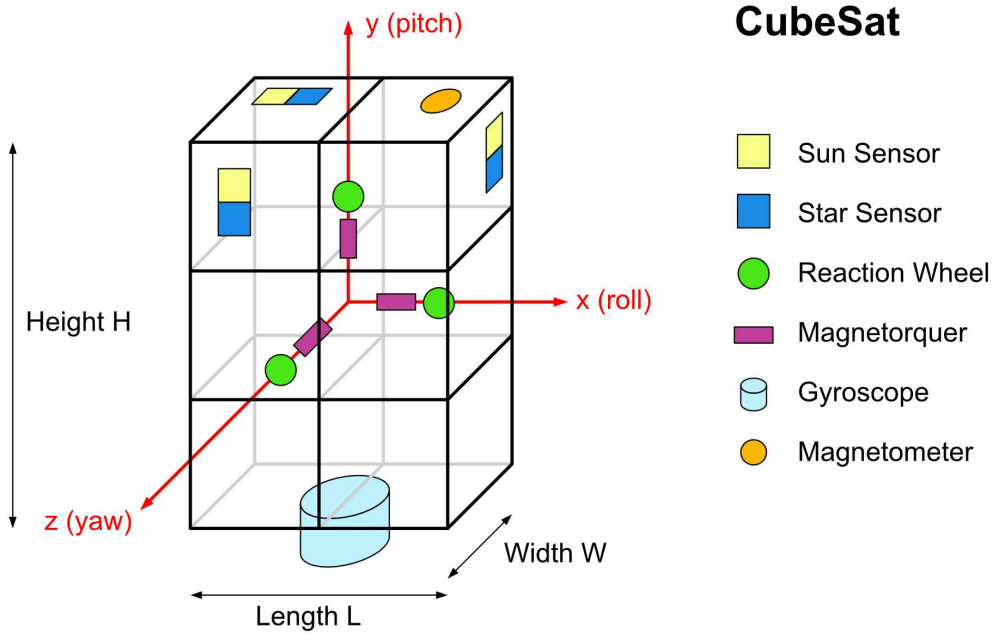

Figure 3.2 Model of the 6UCubeSat

The simulation framework is divided into several Python files, each containing specific classes and functions required for the simulation. The main components include:

- **Main.py**: The main script runs the simulation.
- **PropagationwithAttitude.py**: Contains the spacecraft dynamics models, including the Satellite where the technical datas are defined. This file also specifies the `Meteoroid` class, which is used later in the simulation for the pointing maneuver.
- **Disturbances.py**: Implements various disturbance models acting on the CubeSat in the Disturbances class.
- **Sensors.py**: Includes the Sensors class for attitude determination, incorporating noise into the measurements.
- **Actuators.py**: Contains the class Actuator with models and control laws for detumbling and pointing maneuvers.

Each file is structured to ensure modularity and maintainability by encompassing specific aspects of the ADCS simulation. The classes and functions are designed to interact seamlessly and allow flexible changes and extensions to the simulation framework.

3.2 Orbital and Attitude Determination

In this section, the orbit and attitude propagation of the satellite are described in detail using a comprehensive simulation framework. The original orbit propagation code was already implemented and can be found in [18].

The Earth-centered inertial (ECI)-frame and the body-fixed frame were used for the calculation. The ECI-frame is located at the center of the Earth, translates around the sun with the solar system, and does not rotate [10]. The axis can be seen in Figure 3.3.

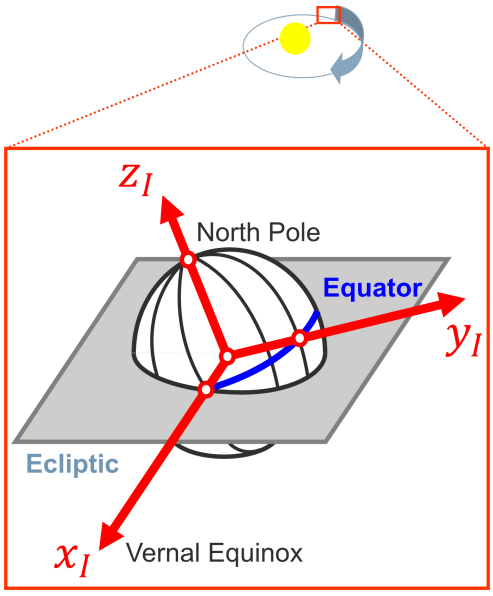

Figure 3.3 Earth-Centered Inertial Frame [10]

The body-fixed frame has its origin in the center of the satellite and consists of the roll, pitch, and yaw axis, as shown in Figure 3.2.

For the initial orbital parameters, the following values were assumed, given in Table 3.2.

Parameter	Value
Semimajor Axis (a)	7070 km
Eccentricity (e)	0.001
True Anomaly (θ)	0 rad
Argument of Perigee (ω)	0
Right Ascension of the Ascending Node (RAAN, Ω)	0

Table 3.2 Parameters for Orbital Propagation

The propagation of the orbit is based on the integration of the true anomaly θ, which is defined as the angle between the current position of the satellite and the direction of the periapsis. The rate of change of θ, denoted as $\dot{\theta}$, is given by

$$\dot{\theta} = \sqrt{1-e^2} \cdot \frac{n}{1 - e\cos(E)}, \tag{3.1}$$

where n is the mean motion, e is the eccentricity, and E is the eccentric anomaly. The second part involves the derivation of the eccentric anomaly. The eccentric anomaly E is calculated using Kepler's law

$$E = \operatorname{atan2}\left(\frac{\sqrt{1-e^2}\sin(\theta)}{e + \cos(\theta)}\right). \tag{3.2}$$

The mean motion n is derived by

$$n = \sqrt{\frac{\mu}{a^3}} \tag{3.3}$$

where μ is the standard gravitational parameter for Earth, which is $3.986004418 \times 10^{14}\ \frac{\mathrm{m}^3}{\mathrm{s}^2}$ and a is the semimajor axis of the orbit. In this thesis, $\dot{\theta}$ is integrated discretely by multiplying it with the times step (Δt) and adding it to the previous value of the true anomaly

$$\theta_{\mathsf{new}} = \theta_{\mathsf{old}} + \dot{\theta} \cdot \Delta t. \tag{3.4}$$

This process ensures that the orbit is accurately propagated over time.

To determine the position of the CubeSat, the position vector $\mathbf{r}_n$ in the inertial frame can be written as

$$\mathbf{r}_{\mathsf{n}} = r \begin{pmatrix} \cos(\Omega)\cos(\omega+\theta) - \sin(\Omega)\sin(\omega+\theta)\cos(i) \\ \sin(\Omega)\cos(\omega+\theta) + \cos(\Omega)\sin(\omega+\theta)\cos(i) \\ \sin(\omega+\theta)\sin(i) \end{pmatrix}, \tag{3.5}$$

where Ω is the right ascension of the ascending node, i is the inclination and ω the argument of perigee.

Hereby, the radius r of the satellite's orbit is determined as

$$r(\theta) = \frac{a\left(1-e^2\right)}{1 + e\cos(\theta)}. \tag{3.6}$$

The velocity vector $\mathbf{v}_N$ in the inertial frame is calculated as follows

$$\mathbf{v}_N = \frac{nr}{\sqrt{1-e^2}} \begin{pmatrix} -\left(\cos(\Omega)\sin(\omega+\theta) + \sin(\Omega)\cos(\omega+\theta)\cos(i)\right) \\ \sin(\Omega)\sin(\omega+\theta) - \cos(\Omega)\cos(\omega+\theta)\cos(i) \\ \sin(i) \end{pmatrix}. \tag{3.7}$$

The calculations use two different coordinate frames: the ECI frame, which is fixed at the center of the Earth and does not rotate with it, and the body-fixed frame, (B)-frame, which is fixed to the center of the spacecraft.

For the determination of attitude, the angular velocity $\boldsymbol{\omega}_B$ is calculated in the Body-fixed frame with respect to the ECI frame by integrating Euler's equation 2.3. For the implementation discussed in this

chapter, the Euler equation is adjusted by adding the terms $\mathbf{M}_{dis}$ for the disturbance torque and $\mathbf{u}_{real}$ for the actual control torque. The modified Euler equation then results as

$$I\dot{\boldsymbol{\omega}} = \mathbf{M}_{dis} + \mathbf{u}_{real} + \boldsymbol{\omega} \times (I\boldsymbol{\omega}). \tag{3.8}$$

Analogous to the integration of θ, as shown in Equation 3.4, the angular velocity is calculated at each time step with

$$\dot{\boldsymbol{\omega}}_{B,new} = \boldsymbol{\omega}_{B,old} + \dot{\boldsymbol{\omega}}_B \cdot \Delta t. \tag{3.9}$$

In the simulation, rotation quaternions are used to propagate the attitude. These are an alternative to rotation matrices for representing rotations in three dimensions. A quaternion consists of four elements and is expressed as

$$\mathbf{q} = q_0 + \mathbf{i}q_1 + \mathbf{j}q_2 + \mathbf{k}q_3, \tag{3.10}$$

where q_0, q_1, q_2 and q_3 are real numbers, whereas $\mathbf{i}, \mathbf{j}$ and $\mathbf{k}$ are imaginary unit vectors, which are orthogonal towards each other. However, to simplify, only the four coefficients are used to specify a quaternion, as shown in the following form

$$\mathbf{q} = (q_0, q_1, q_2, q_3). \tag{3.11}$$

To ensure valid rotations, quaternions are normalized, maintaining the unit length condition

$$\|\mathbf{q}\| = 1. \tag{3.12}$$

Although using quaternions is less intuitive, they are computationally efficient as they reduce complex trigonometric operations to simple multiplication and addition and avoid singularities. [23]

The rate of change of a quaternion, $\dot{\mathbf{q}}$, is given by

$$\dot{\mathbf{q}} = \frac{1}{2}\mathbf{q} \otimes \boldsymbol{\omega}, \tag{3.13}$$

where $\otimes$ denotes quaternion multiplication and ω is the angular velocity, which is represented as a quaternion $[0, \omega_x, \omega_y, \omega_z]$. The quaternion derivative $\dot{\mathbf{q}}$ is calculated as follows

$$\dot{\mathbf{q}} = \frac{1}{2}\begin{bmatrix} q_0 & -q_1 & -q_2 & -q_3 \\ q_1 & q_0 & -q_3 & q_2 \\ q_2 & q_3 & q_0 & -q_1 \\ q_3 & -q_2 & q_1 & q_0 \end{bmatrix} \begin{bmatrix} 0 \\ \omega_x \\ \omega_y \\ \omega_z \end{bmatrix}. \tag{3.14}$$

Using this formula, the quaternion is updated at each time step

$$\mathbf{q}_{new} = \mathbf{q}_{old} + \dot{\mathbf{q}} \cdot \Delta t. \tag{3.15}$$

After each update, the quaternion is normalized to maintain its unit length.

Because rotation matrices provide a more intuitive representation of orientations, converting quaternions to rotation matrices simplifies the interpretation of results in various applications. The rotation matrix $\mathbf{A}_{BN}$, which represents the transformation from the inertial system to the body-fixed system, is derived from the quaternion components as follows

$$\mathbf{A}_{BN} = \begin{bmatrix} 1-2(q_2^2+q_3^2) & 2(q_1q_2-q_0q_3) & 2(q_0q_2+q_1q_3) \\ 2(q_1q_2+q_0q_3) & 1-2(q_1^2+q_3^2) & 2(q_2q_3-q_0q_1) \\ 2(q_1q_3-q_0q_2) & 2(q_0q_1+q_2q_3) & 1-2(q_1^2+q_2^2) \end{bmatrix}. \tag{3.16}$$

To calculate the rotation matrix $\mathbf{A}_{LN}$, which represents the transformation from the inertial frame to the local orbital frame, the following steps are used:

The matrix $\mathbf{A}_1$ is calculated using the true anomaly angle, θ

$$\mathbf{A}_1 = \begin{bmatrix} \cos(\theta) & \sin(\theta) & 0 \\ -\sin(\theta) & \cos(\theta) & 0 \\ 0 & 0 & 1 \end{bmatrix}. \tag{3.17}$$

Then, the matrix $\mathbf{A}_2$ is calculated using the inclination angle i

$$\mathbf{A}_2 = \begin{bmatrix} 1 & 0 & 0 \\ 0 & \cos(i) & \sin(i) \\ 0 & -\sin(i) & \cos(i) \end{bmatrix}. \tag{3.18}$$

The product of these matrices gives the rotation matrix $\mathbf{A}_{LN}$

$$\mathbf{A}_{LN} = \mathbf{A}_1 \mathbf{A}_2. \tag{3.19}$$

This is needed for the calculation of the Gravity-Gradient Torque, explained in section 3.3.4

3.3 Implementation of Disturbances

This section provides an overview of the equations and implementation of the disturbances. There are several disturbances acting on a spacecraft in orbit, of which the four most influential for Earth-orbiting are modeled. These are solar radiation pressure torques $\mathbf{M}_{SRP}$, gravity-gradient effects $\mathbf{M}_{GG}$, aerodynamic torques $\mathbf{M}_{drag}$, and torques caused by the Earth's magnetic field $\mathbf{M}_{mag}$, which only play a significant role in low-altitude orbits. [14]

The different disturbance torques are summarized, resulting in the total disturbance torque $\mathbf{M}_{dis}$ as follows.

$$\mathbf{M}_{dis} = \mathbf{M}_{SRP} + \mathbf{M}_{drag} + \mathbf{M}_{mag} + \mathbf{M}_{GG} \tag{3.20}$$

Figure 3.4 shows the disturbances evaluated over two orbital periods for a time step of $\Delta t = 1s$. The combination of all disturbance torques reaches a maximum magnitude of 1.4×10^{-6}.

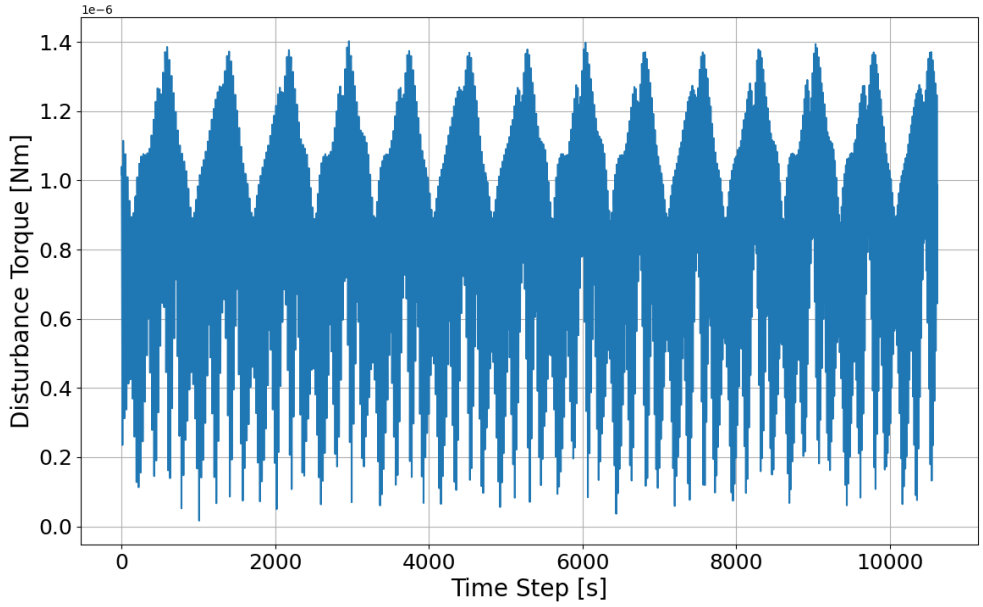

Figure 3.4 Total Disturbance Torque (Time Step = 1s)

3.3.1 Solar Radiation Pressure

Solar radiation encompasses the full spectrum of electromagnetic waves, that are emitted by the Sun. In addition to this, the Sun expels particulate radiation, called solar wind, which is composed mainly of ionized nuclei and electrons. Both effects can produce a torque on the spacecraft. However, the solar radiation is much stronger and therefore, the solar wind was neglected in this model. [29]

For the calculation, there are several values of importance, which are provided in table 3.3.

Parameter	Description	Value
Fe	Direct solar radiation	$1367\,\mathrm{W/m^2}$
c	Speed of light	3×10^8 m/s
ρ_s	Specular reflectivity	0.5
ρ_d	Diffuse reflectivity	0.1
$\mathbf{S}_B$	unit vector from the plate center of pressure to the Sun	$[1,1,1]^T$

Table 3.3 Parameters for Calculation of Solar Radiation Pressure

The specular and diffuse reflectivities depend on the material of the surface of the spacecraft [23]. As a simplification, the vector representing the position of the Sun in the body-fixed frame $\mathbf{S}_B$ is considered fixed.

The solar radiation force $F_{SRP,i}$ is calculated by

$$\mathbf{F}_{SRP,i} = -\frac{Fe}{c} \cdot A_i \cdot (\hat{\mathbf{S}}_b \cdot \mathbf{n}_i) \cdot \left[(1-\rho_s) \cdot \hat{\mathbf{S}}_b + \left(2\rho_s (\hat{\mathbf{S}}_b \cdot \mathbf{n}_i) + \frac{2}{3}\rho_d \right) \cdot \mathbf{n}_i \right]. \tag{3.21}$$

$\hat{\mathbf{S}}_b$ is the normalized vector of $\mathbf{S}_b$. A_i represents the corresponding surface area of the satellite. There are three different surface areas calculated based on the dimensions of the satellite, each of which appears twice, resulting in a total of six surfaces. These dimensions are provided in Table 3.1. Accordingly, the surface areas are determined by

$$\begin{aligned} A_1 &= h \cdot w \\ A_2 &= l \cdot w \,. \\ A_3 &= h \cdot l \end{aligned} \tag{3.22}$$

The normal vectors $\mathbf{n}_i$ for each surface are given in Equation 3.23.

$$\begin{aligned} \mathbf{n}_1 &= [1,0,0]^T, \quad \mathbf{n}_{-1} = [-1,0,0]^T \\ \mathbf{n}_2 &= [0,1,0]^T, \quad \mathbf{n}_{-2} = [0,-1,0]^T \\ \mathbf{n}_3 &= [0,0,1]^T, \quad \mathbf{n}_{-3} = [0,0,-1]^T \end{aligned} \tag{3.23}$$

For results greater than zero when multiplying the normal vector $\mathbf{n}_i$ with the normalized Sun vector $\hat{\mathbf{S}}_b$, the torque component $\mathbf{M}_{SRP,i}$ results as

$$\mathbf{M}_{SRP,i} = \mathbf{r}_i \times \mathbf{F}_{SRP,i}, \tag{3.24}$$

with $\mathbf{r}_i$ as the relative position vector and $\mathbf{F}_i$ as the force. Otherwise, the torque component $\mathbf{M}_{SRP,i}$ is set to a vector composed of zeros. The total disturbance torque $\mathbf{M}_{SRP}$ is the sum of the calculation for each surface

$$\mathbf{M}_{SRP} = \sum_i \mathbf{M}_{SRP,i}. \tag{3.25}$$

In the simulation, the solar radiation pressure torque is calculated for each time step. The magnitude of the torque evaluated with the initial condition $\boldsymbol{\omega}_0 = [5,10,-7]^T$ °/s, over two orbital periods and with a time step of $\Delta t = 1s$, is around $8.37 \times 10^{-9} Nm$. This value is constant, as it only changes with the direction of the Sun's position $\hat{\mathbf{S}}_b$, which is assumed to be fixed.

3.3.2 Drag

In low Earth orbit, air drag significantly affects spacecraft attitude. The disturbance torque due to air drag is computed using the spacecraft's relative velocity concerning the atmosphere, the surface areas exposed to the flow, and the spacecraft's aerodynamic properties.

The following variables in table 3.4 have been used for the calculations and are assumed constant.

Parameter	Description	Value
ρ	Atmospheric Density	3.725×10^{-12} kg/m^3
C_D	Drag Coefficient	2.2

Table 3.4 Parameters for Calculation of Air-Drag

The aerodynamic force $\mathbf{F}_{drag,i}$ is calculated in the simulation by the formula

$$\mathbf{F}_{drag,i} = -0.5 \cdot C_D \cdot \rho \cdot (\|\mathbf{v}_{rel,B}\|)^2 \cdot (\mathbf{n}_i \cdot \hat{\mathbf{v}}_{rel,B}) \cdot A_i \cdot \hat{\mathbf{v}}_{rel,B}. \tag{3.26}$$

The surface areas used for the calculations are equal to equation 3.22, as well as the unit vectors orthogonal on the surfaces (refer to equation 3.23). The $v_{rel,B}$ is the relative velocity of the spacecraft in the body-fixed frame.

At first, the orbit is propagated as described in chapter 3.2 to get the position and velocity in the ECI frame. Then the relative velocity is calculated by

$$\mathbf{v}_{rel,N} = \mathbf{v}_{ECI} + \boldsymbol{\omega}_E \times \mathbf{r}_{ECI}. \tag{3.27}$$

Afterwards, using the $\mathbf{A}_{BN}$ from Equation 3.16, it is converted to the body-fixed frame

$$\mathbf{v}_{rel,B} = \mathbf{A}_{bn} \cdot \mathbf{v}_{rel,N}. \tag{3.28}$$

To compute the disturbance torque, the cross product of the position vector $\mathbf{r}_i$ and the force $\mathbf{F}_i$ is evaluated. The total atmospheric disturbance torque $\mathbf{M}_{drag}$ results as

$$\mathbf{M}_{drag} = \begin{cases} \sum_{i=1}^{N} \mathbf{r}_i \times \mathbf{F}_{drag,i} & \text{if } \hat{\mathbf{n}}_\mathbf{i} \cdot \hat{\mathbf{v}}_{\mathbf{rel,B}} > 0 \\ \mathbf{0} & \text{if } \hat{\mathbf{n}}_i \cdot \hat{\mathbf{v}}_{rel,B} \leq 0. \end{cases} \tag{3.29}$$

Here $\mathbf{r}_i$ is equal to the position vector used for the solar radiation pressure.

In the Python script, it is calculated for each time step $\Delta t = 1s$ over two orbital periods, which is depicted in Figure 3.5. The magnitude of the drag torque $\mathbf{M}_{drag}$ corresponds to an order of magnitude of 10^{-7} Nm.

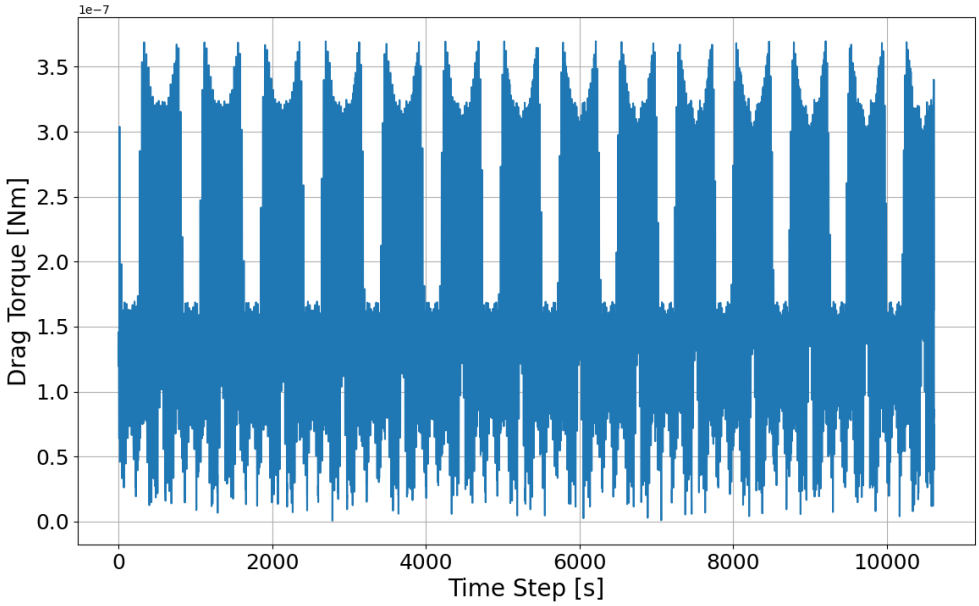

Figure 3.5 Drag Torque over two Orbital Periods (Time Step = 1s)

3.3.3 Magnetic Field Torque

The magnetic torque disturbance is produced by the Earth's Magnetic field acting on the satellite. To simulate this disturbance, the magnetic field is calculated using the magnetic dipole approximation. The values provided in Table 3.5 are used for this calculation.

Parameter	Description	Value
g_{10}	Gaussian Coefficient g_{10}	$-29,682 \times 10^{-9}$
g_{11}	Gaussian Coefficient g_{11}	$-1,788 \times 10^{-9}$
h_{11}	Gaussian Coefficient h_{11}	$5,318 \times 10^{-9}$
H_0	Computed Constant H_0	$\sqrt{g_{10}^2 + g_{11}^2 + h_{11}^2}$

Table 3.5 Parameters for Calculation of Magnetic Torque

For the calculation of the magnetic field in the inertial frame $\mathbf{b}_N$, the following equation is used

$$\mathbf{b}_N = \frac{R_E^3 H_0}{r_n^3} \left(3(\mathbf{m} \cdot \hat{\mathbf{r}}_n)\hat{\mathbf{r}}_n - \mathbf{m}\right). \tag{3.30}$$

The magnetic moment $\mathbf{m}$ is calculated by

$$\mathbf{m} = \begin{bmatrix} \sin 11.5° \cos \omega_E t \\ \sin 11.5° \sin \omega_E t \\ \cos 11.5° \end{bmatrix}. \tag{3.31}$$

where the time t is assumed constant and equals 1 second. The position vector in the ECI frame $\mathbf{r}_n$ is evaluated by the orbit propagation (Section 3.2) and by dividing it by its magnitude, the versor $\hat{\mathbf{r}}_n$ is obtained. H_0 represents a constant evaluated by the Gaussian coefficients. After obtaining $\mathbf{b}_n$, it is converted to the body-fixed-frame by

$$\mathbf{b}_B = \mathbf{A}_{bn}\mathbf{b}_N. \tag{3.32}$$

The magnetic field in the body frame $\mathbf{b}_B$ is first determined to calculate the disturbance torque due to the Earth's magnetic field. Then, the cross product of the spacecraft's magnetic moment $\mathbf{m}$ and $\mathbf{b}_B$ is computed to get the magnetic disturbance torque $\mathbf{M}_{Mag}$

$$\mathbf{M}_{mag} = \mathbf{m} \times \mathbf{b}_B. \tag{3.33}$$

In Figure 3.6, two orbital periods are depicted of the magnetic torque $\mathbf{M}_{mag}$. The order of magnitude is around 10^{-6} Nm.

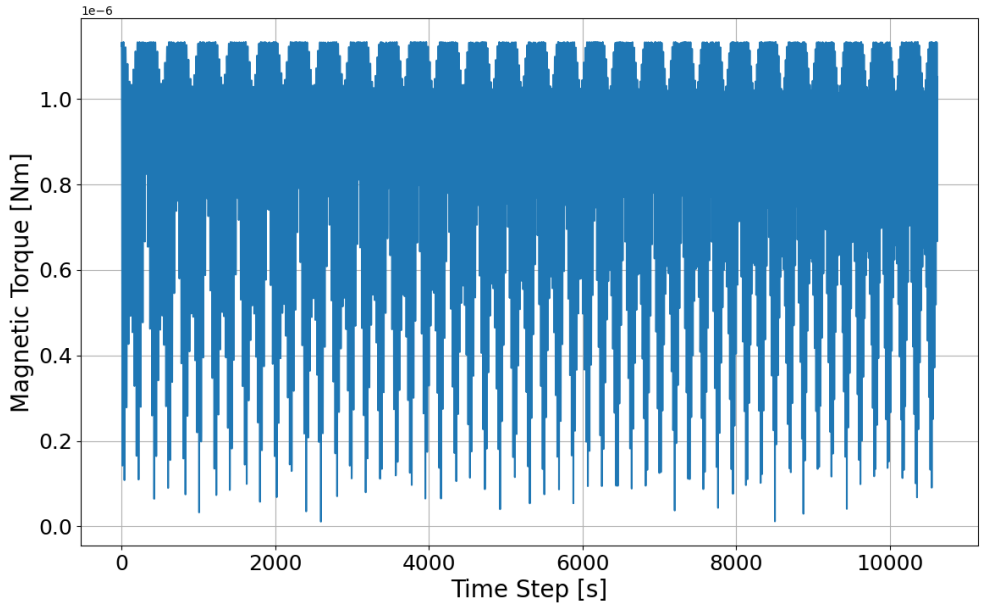

Figure 3.6 Magnetic Torque over two Orbital Periods (Time Step = 1s)

3.3.4 Gravity-Gradient Torque

Calculating the torque by the gravity gradient requires the following data presented in table 3.6.

Parameter	Description	Value
m_{earth}	Mass of the Earth	6.972×10^{24} kg
G	Gravitational Constant	6.67408×10^{-11} m^{3}kg^{-1}s^{-2}

Table 3.6 Parameters for Gravitational Calculations

By the propagation with orbit, the position vector in the inertial frame $\mathbf{r}_n$ is obtained, which is transformed to the body frame using the rotation matrix $\mathbf{A}_{BN}$, resulting in

$$\mathbf{r}_b = \mathbf{A}_{BN}\mathbf{r}_n. \tag{3.34}$$

The length of the position vector in the body-fixed frame r is determined by

$$r = \sqrt{\mathbf{r}_b \cdot \mathbf{r}_b}, \tag{3.35}$$

and is needed for the calculation of the gravity-gradient torque

$$\mathbf{M}_{GG} = \begin{bmatrix} M_{GG,x} \\ M_{GG,y} \\ M_{GG,,z} \end{bmatrix} = \frac{3Gm_{earth}}{r^3} \begin{bmatrix} \frac{(I_z - I_y)}{I_x} c_3 c_2 \\ \frac{(I_x - I_z)}{I_y} c_1 c_3 \\ \frac{(I_y - I_x)}{I_z} c_2 c_1 \end{bmatrix}. \tag{3.36}$$

The vector $[1, 0, 0]^T$ is transformed to obtain the components c_1, c_2, and c_3

$$\begin{bmatrix} c_1 \\ c_2 \\ c_3 \end{bmatrix} = \mathbf{A}_{BL} \begin{bmatrix} 1 \\ 0 \\ 0 \end{bmatrix}, \tag{3.37}$$

where $\mathbf{A}_{BL}$ is obtained by

$$\mathbf{A}_{BL} = \mathbf{A}_{BN}\mathbf{A}_{LN}^T. \tag{3.38}$$

In Figure 3.7 the Gravity Gradient Torque is shown over two orbital periods. The order of magnitude is 10^{-7} Nm.

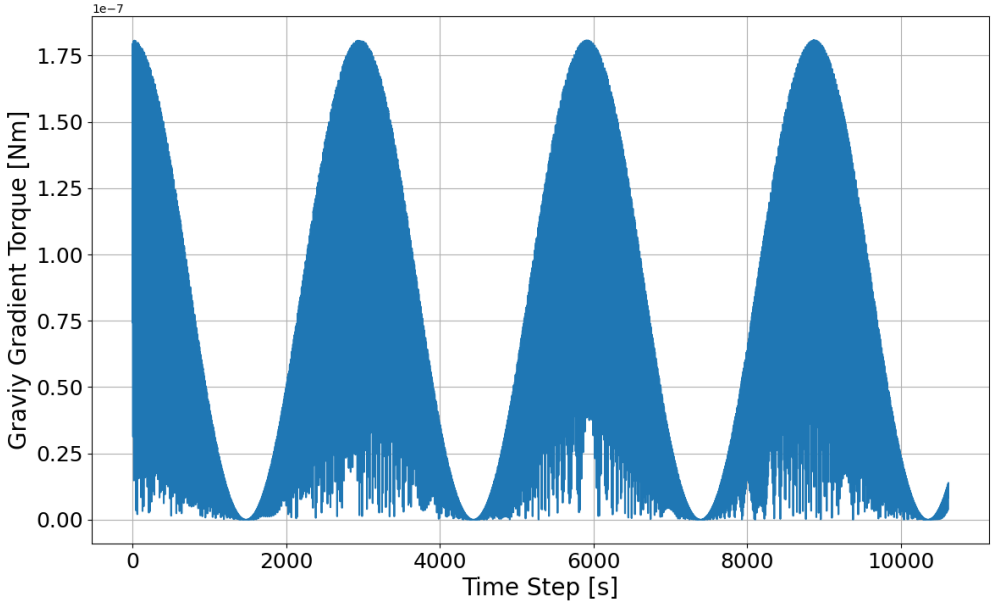

Figure 3.7 Gravity Gradient Torque over two Orbital Periods (Time Step = 1s)

3.4 Implementation of Sensors

The sensors are responsible for the attitude determination as described in Section 2.2.1. In the simulation, noise was added to the data from the gyroscope, the Star sensor, and the Sun sensor to account for real-life effects on the sensors. The gyroscope takes Angle Random Walk (ARW) and Rate Random Walk (RRW) into account, while the Star and Sun sensors introduce Gaussian noise into the attitude measurements. The values for standard deviations are provided in Table 3.7.

Sensor	**Noise Type**	**Standard Deviation (degree)**
Gyroscope	Angle Random Walk (ARW)	$\left(\frac{0.2}{3600}\right)^2$
Gyroscope	Rate Random Walk (RRW)	$\left(\frac{0.3}{3600}\right)^2$
Star Sensor	Gaussian Noise	0.01
Sun Sensor	Gaussian Noise	0.5

Table 3.7 Sensor Noise Parameters

The Star sensor has better accuracy than the Sun sensor, which is reflected in the lower standard deviation.

The noise of the Star and Sun sensors is given in the Euler angles ϕ, θ and ψ. These angles describe the small random errors in the measured orientation, representing inaccuracies in the sensors' ability to determine the spacecraft's roll, pitch, and yaw angles. The noise vector is generated using a random function with a mean of zero and specified standard deviation values. The generated noise is then added to the rotation matrix $\mathbf{A}_{BN}$ and normalized to ensure the resulting matrix maintains its orthogonality and unit determinant.

To add the noise to the $\mathbf{A}_{BN}$, the noise has to be converted from the Euler angles to the rotation matrix by the formula

$$\mathbf{R} = \begin{bmatrix} \cos\theta\cos\psi & -\cos\phi\sin\psi + \sin\phi\sin\theta\cos\psi & \sin\phi\sin\psi + \cos\phi\sin\theta\cos\psi \\ \cos\theta\sin\psi & \cos\phi\cos\psi + \sin\phi\sin\theta\sin\psi & -\sin\phi\cos\psi + \cos\phi\sin\theta\sin\psi \\ -\sin\theta & \sin\phi\cos\theta & \cos\phi\cos\theta \end{bmatrix}. \tag{3.39}$$

Here, the noise is added to the equation 3.16.

Alternatively, the noise could also be converted to the quaternions with the formula

$$q_0 = \cos\left(\frac{\phi}{2}\right)\cos\left(\frac{\theta}{2}\right)\cos\left(\frac{\psi}{2}\right) + \sin\left(\frac{\phi}{2}\right)\sin\left(\frac{\theta}{2}\right)\sin\left(\frac{\psi}{2}\right) \tag{3.40a}$$

$$q_1 = \sin\left(\frac{\phi}{2}\right)\cos\left(\frac{\theta}{2}\right)\cos\left(\frac{\psi}{2}\right) - \cos\left(\frac{\phi}{2}\right)\sin\left(\frac{\theta}{2}\right)\sin\left(\frac{\psi}{2}\right) \tag{3.40b}$$

$$q_2 = \cos\left(\frac{\phi}{2}\right)\sin\left(\frac{\theta}{2}\right)\cos\left(\frac{\psi}{2}\right) + \sin\left(\frac{\phi}{2}\right)\cos\left(\frac{\theta}{2}\right)\sin\left(\frac{\psi}{2}\right) \tag{3.40c}$$

$$q_3 = \cos\left(\frac{\phi}{2}\right)\cos\left(\frac{\theta}{2}\right)\sin\left(\frac{\psi}{2}\right) - \sin\left(\frac{\phi}{2}\right)\sin\left(\frac{\theta}{2}\right)\cos\left(\frac{\psi}{2}\right). \tag{3.40d}$$

3.5 Implementation of Actuators

As mentioned in Section 3.1, the actuators consist of three magnetic torques and three reaction wheels. Typical values for the actuators can be found in the datasheet [7].

In this simulation relevant values for the magnetorquers were assumed and are displayed in Table 3.5.

Parameter	Symbol	Value
Number of turns of wires	N	500
Current	I	$0.1A$
Diameter of the coil	d	$0.05m$

Table 3.8 Parameters of Magnetorquers

The magnetic dipole moment m is calculated by the equation 2.4.

In addition, a three-wheel configuration was chosen for the reaction wheels. This choice enables full three-axis control through the use of three orthogonal reaction wheels. This arrangement provides precise control over the orientation of the satellite and enables nadir, sun, and inertial pointing. The specifications were also assumed for the reaction wheels and are detailed in Table 3.9.

Parameter	Symbol	Value
Max Speed	$\omega_{RW,max}$	$5000RPM$
Max Momentum Storage of Reaction Wheel	$h_{RW,max}$	$50mNms$
x-Position	x_{RW}	0.05 m
y-Position	y_{RW}	0.075 m
z-Position	z_{RW}	0.05 m

Table 3.9 Values of Reaction Wheels

The magnetic dipole moment generated by each magnetorquer is a vector quantity. The direction of the magnetic moment must be considered.

The produced torque is calculated accordingly to equation 2.5. The magnetic field is simulated, as described in Section 3.3.3.

The reaction wheel model 3x CW0162 has been chosen for this mission, which is suitable for the 6U satellite configuration. The torque produced by the reaction wheels is essential for controlling the satellite's orientation. This torque is derived from the angular momentum exchange between the reaction wheels and the satellite. The angular momentum $\mathbf{h}$ for both the satellite and reaction wheel is given by the formula

$$\mathbf{h}_{RW} = I_{RW}\boldsymbol{\omega}_{RW}, \tag{3.41}$$

where I is the moment of inertia and $\boldsymbol{\omega}$ the angular velocity.

Assuming $\mathbf{I}_{RW}$ is constant, the relationship between the desired angular momentum and angular velocity and the maximum angular momentum and angular velocity can be expressed as

$$\frac{\mathbf{h}_{RW,des}}{\omega_{RW,des}} = \frac{\mathbf{h}_{RW,max}}{\omega_{RW,max}}. \tag{3.42}$$

This can be rearranged to solve for the desired angular momentum

$$\mathbf{h}_{RW,des} = \frac{\mathbf{h}_{RW,max}}{\omega_{RW,max}}\omega_{RW,des}. \tag{3.43}$$

The force is given by the derivation of the angular momentum

$$\dot{\mathbf{h}} = \mathbf{F}. \tag{3.44}$$

In this thesis, the derivation of the force is simplified by dividing it by the time step Δt

$$\mathbf{F} = \frac{\mathbf{h}}{\Delta t}, \tag{3.45}$$

which provides a practical way to calculate the force applied by the reaction wheels during each control cycle.

The torque is calculated by

$$\mathbf{u}_{RW} = \mathbf{F}\mathbf{d}, \tag{3.46}$$

where d is the distance from the positions of the reaction wheels to the center of mass of the satellite.

3.6 Control Laws

The goal of the ADCS is to detumble the satellite and then point at a meteoroid and track it. These maneuvers are realized by the control law. In the following Sections, the control strategies for detumbling and pointing, as well as the implementation in the code, are explained.

3.6.1 Detumbling

The magnetorquers generate a magnetic moment $\mathbf{m}$ as shown in Section 3.5. The direction of the necessary control torque depends on the direction of the Earth's magnetic field $\mathbf{B}$ and the current angular velocity of the satellite $\boldsymbol{\omega_{sat}}$. The cross-product

$$\mathbf{B} \times \boldsymbol{\omega}_{sat} \tag{3.47}$$

provides a vector perpendicular to both $\mathbf{B}$ and $\boldsymbol{\omega_{sat}}$, which indicates the direction in which the torque should be applied to counteract the angular velocity.

The magnetic dipole moment in the code is calculated by

$$\mathbf{m} = \mathbf{S}m, \tag{3.48}$$

while $\mathbf{S}$ is just a selection vector, which defines the direction of the needed torque, since there are three magnetorquers, which can all produce the same magnetic dipole in the corresponding direction

This vector $\mathbf{S}$ is set based on the sign of each component of the cross-product

$$S_i = \begin{cases} 1 & \text{if } (\mathbf{B} \times \boldsymbol{\omega})_i < 0 \\ 0 & \text{if } (\mathbf{B} \times \boldsymbol{\omega})_i = 0 \\ -1 & \text{if } (\mathbf{B} \times \boldsymbol{\omega})_i > 0 \end{cases}. \tag{3.49}$$

The torque ($\mathbf{u}_{MT}$) generated by the magnetorquers is calculated with the equation 3.48 and by

$$\mathbf{u}_{MT} = \mathbf{m} \times \mathbf{B}. \tag{3.50}$$

For the satellite, the angular momentum must balance the angular momentum of the reaction wheels

$$\mathbf{I}_{sat}\boldsymbol{\omega}_{sat} = -\mathbf{I}_{RW}\boldsymbol{\omega}_{RW}. \tag{3.51}$$

The reaction wheels generate control torques by spinning at varying speeds. The torque produced by a reaction wheel, therefore, is proportional to its angular momentum and its angular velocity.

The torque generated by the reaction wheels $\mathbf{u}_{RW}$ is calculated based on the satellite's angular velocity and the maximum torque the wheels can produce. The torque is applied in the opposite direction of the angular velocity to reduce the rotation. The torque generated by a reaction wheel $\mathbf{u}_{RW}$ can be expressed as

$$u_{RW,i} = \begin{cases} -\frac{M_{RW,\text{max}}}{\omega_{RW,\text{max}}} \cdot \omega_i \cdot 100 \cdot d_i & \text{if } |\omega_i| > \omega_{\text{threshold}} \\ 0 & \text{if } |\omega_i| \leq \omega_{\text{threshold}} \end{cases}, \tag{3.52}$$

where d_i is the distance from the position of each reaction wheel to the center of mass and $\omega_{threshold}$ is the threshold angular velocity below which the reaction wheels do not apply torque. The threshold angular velocity is set to $0.05\frac{rad}{s}$, which has proven to be the most efficient value. The factor 100 is the control gain applied to modulate the torque based on the angular velocity.

As there are three reaction wheels on each axis, the torque is calculated for the three components with the corresponding positions of the reaction wheels. This control strategy ensures that the torque is applied to reduce the satellite's angular velocity effectively.

The control torque is then calculated by

$$\mathbf{u}_{real} = \mathbf{u}_{MT} + \mathbf{u}_{RW}, \tag{3.53}$$

and added to the equation 3.8.

In this simulation, the control torque $\mathbf{u}_{real}$ is applied in the Propagation of attitude to the $\dot{\omega}$, resulting in

$$\dot{\omega} = \mathbf{I}^{-1} \cdot (\mathbf{M}_{\text{dis}} + \mathbf{u}_{\text{real}} + \omega \times (\mathbf{I} \cdot \omega)). \tag{3.54}$$

3.6.2 Pointing Algorithms

This section explains the process of pointing a meteoroid using only reaction wheels. For the pointing algorithm, a meteoroid was initialized with the data provided in Table 3.10.

Parameter	Symbol	Value
Initial Position	$\mathbf{r}^N_{0,met}$	$[7078000, 0, 0]$ m
Initial Velocity	$\mathbf{v}^N_{0,met}$	$[0, 0, 0]$ m/s

Table 3.10 Initial Conditions of the Meteoroid in the ECI Frame

To simplify the model, the meteoroid's velocity was assumed to be zero, resulting in a constant position. The pointing direction $\mathbf{d}_{pointing}$ is represented by the third axis of the rotation matrix, which should be aligned with the target, in this case, the meteoroid.

The calculation of the control torque follows a similar approach to the control torque on the detumbling, as described in Section 3.6.1. However, for the pointing maneuver, the condition is based on the angle $\boldsymbol{\theta}$, which defines the angle between the direction of the meteoroid and the current pointing direction in all three dimensions.

The position of the meteoroid with respect to the body-fixed frame is evaluated by obtaining the satellite's position in the ECI-frame $\mathbf{r}_{sat^N}$ through the orbit propagation, see chapter 3.2. The relative position, which represents the relative position between the meteoroid and the satellite in the ECI frame, is calculated by

$$\mathbf{r}_{rel^N} = \mathbf{r}_{met^N} - \mathbf{r}_{sat^N}. \tag{3.55}$$

To determine $\boldsymbol{\theta}$, both vectors $\mathbf{r}_{rel^N}$ and the pointing direction of the satellite $\mathbf{d}_{poiniting}$ has to be normalized resulting in the direction vectors

$$\hat{\mathbf{d}}_{target} = \frac{\mathbf{r}_{rel,N}}{\|\mathbf{r}_{rel,N}\|}, \quad \hat{\mathbf{d}}_{pointing} = \frac{\mathbf{d}_{pointing}}{\|\mathbf{d}_{pointing}\|}. \tag{3.56}$$

The angle between these two vectors is calculated in each direction (x, y and z) by

$$\begin{aligned} \alpha_x &= \arccos(\mathbf{e}_x \cdot \hat{\mathbf{d}}_{pointing}), \quad \beta_x = \arccos(\mathbf{e}_x \cdot \hat{\mathbf{d}}_{target}), \\ \alpha_y &= \arccos(\mathbf{e}_y \cdot \hat{\mathbf{d}}_{pointing}), \quad \beta_y = \arccos(\mathbf{e}_y \cdot \hat{\mathbf{d}}_{target}), \\ \alpha_z &= \arccos(\mathbf{e}_z \cdot \hat{\mathbf{d}}_{pointing}), \quad \beta_z = \arccos(\mathbf{e}_z \cdot \hat{\mathbf{d}}_{target}). \end{aligned} \tag{3.57}$$

Here the $\mathbf{e}_x$, $\mathbf{e}_y$ and $\mathbf{e}_z$ are the unit vectors of the inertial frame. By subtracting these angles, the desired attitude angles $\boldsymbol{\theta}$ are calculated as

$$\boldsymbol{\theta} = \begin{bmatrix} \alpha_x - \beta_x \\ \alpha_y - \beta_y \\ \alpha_z - \beta_z \end{bmatrix}. \tag{3.58}$$

The obtained values are compared to the $\theta_{threshold}$, which is set to 0.05 rad to determine whether the current angles exceed this threshold. The control follows the logic, similar to the detumbling maneuver, described in Section 3.6.1, resulting in the control torque

$$u_{RW,i} = \begin{cases} -\frac{M_{RW,\text{max}}}{\omega_{RW,\text{max}}} \cdot \omega_i \cdot 100 \cdot \cdot d_i & \text{if } |\theta_i| > \theta_{threshold} \\ 0 & \text{if } |\theta_i| \leq \theta_{\text{threshold}} \end{cases}. \tag{3.59}$$

This control torque is again added to equation 3.54, and therefore acts on the angular velocity, accordingly on the $\mathbf{A}_{BN}$, which represents the attitude.

4 Results

In this Section, the simulation explained in Chapter 3 is tested, and the results are discussed. The CubeSat's attitude behavior is analyzed under both ideal circumstances and real circumstances, including noise and disturbances acting on it. Subsequently, the maneuvers for detumbling and pointing are discussed across different test scenarios with various constellations of actuators. The speed of achieving detumbling with different actuators is compared, and the precision of the pointing maneuver is evaluated.

4.1 Effects of Noise and Disturbances

Before examining specific maneuvers, an overview of the conditions under which the simulations were conducted is provided, focusing on the impact of noise and disturbances.

In this case the initial angular velocity was set to

$$\boldsymbol{\omega} = [5, 10, -7]^T \text{°/s}. \tag{4.1}$$

For the simulation and plots, different durations and time steps (Δt) have been used to best depict the results. Given the semimajor axis corresponding to an altitude of 700 km, the orbital period is approximately 88.5 minutes, which is equal to 5310 seconds. The simulation duration is often chosen as a multiple of this orbital period to ensure comprehensive coverage of the satellite's behavior over several orbits.

4.1.1 Ideal Conditions

First, the CubeSat's attitude behavior is evaluated under ideal circumstances, with neither noise nor disturbances acting on the spacecraft. Figure 4.1 depicts the components of the rotation matrix $\boldsymbol{A}_{BN}$ over one orbital period, evaluated with a time step of $\Delta t = 1s$. The matrix converts coordinates from the inertial frame to the body-fixed frame without noise or disturbances. Each line in the plot represents one of the components of the $\boldsymbol{A}_{BN}$.

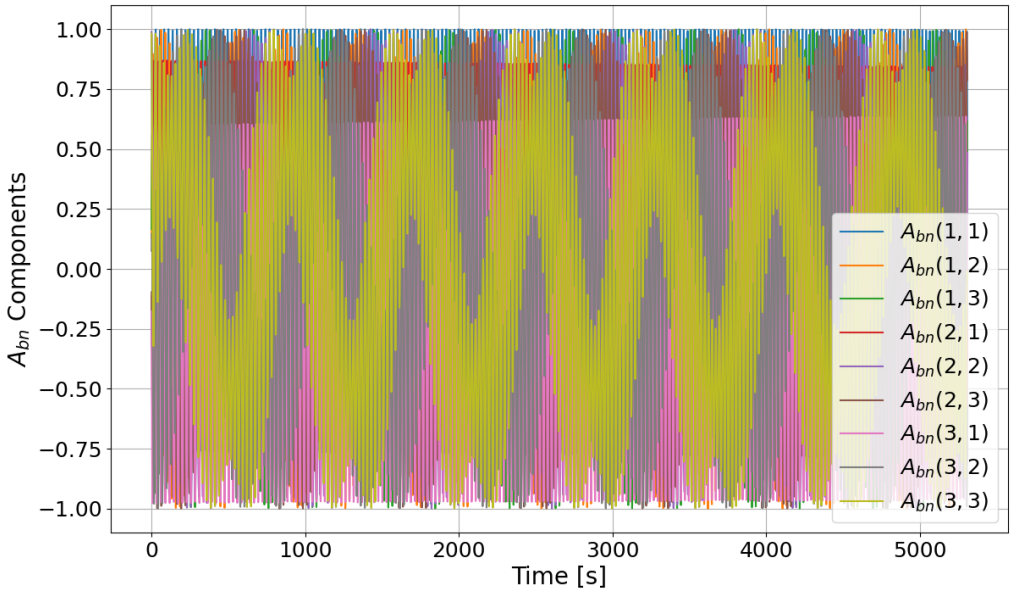

Figure 4.1 Components of the Rotation Matrix $\boldsymbol{A}_{BN}$ without Noise and Disturbances (Time Step = 1s).

The components of the rotation matrix oscillate continuously over time, indicating that the CubeSat maintains a dynamic but stable orientation due to the initial angular velocity. The absence of noise and disturbances allows for a clear observation of the inherent oscillatory behavior of the CubeSat's attitude. The rotation matrix components exhibit periodic behavior with no significant drift over time. This indicates the stability of the simulation and ensures that the rotation matrix and the propagation of attitude are implemented correctly.

In Figure 4.2, for clarity, only the first three values in the first row of the matrix are depicted. The periodicity is clearly visible, with a period of approximately $700s$.

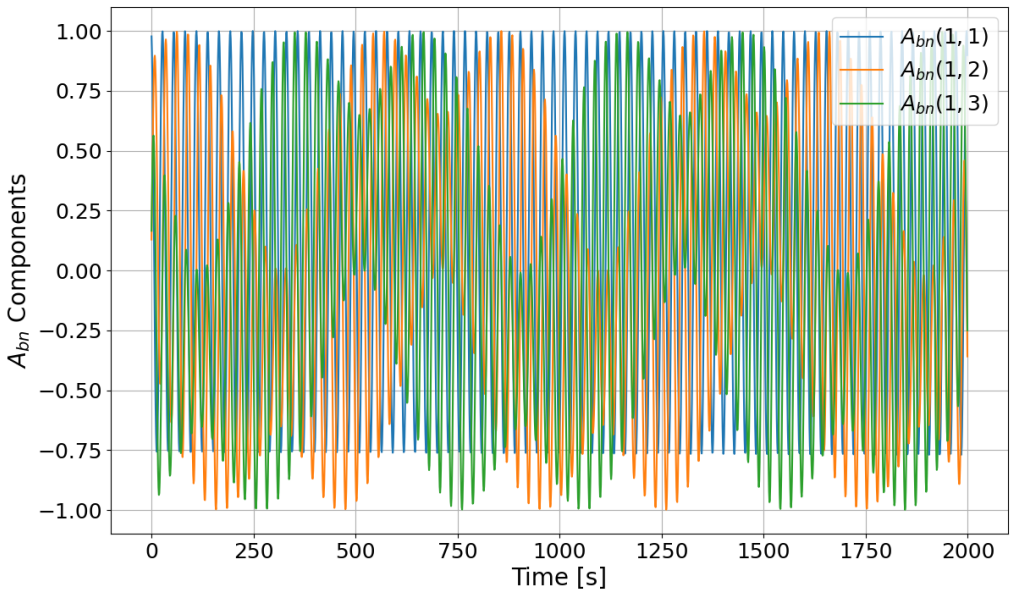

Figure 4.2 Three Components of the Rotation Matrix $\boldsymbol{A}_{BN}$ without Noise and Disturbances (Time Step = 1s).

Similarly, Figure 4.3 displays the components of the quaternions $\mathbf{q}$ without noise and disturbances for one orbital period, with a time step $\Delta t = 1s$. Each line represents one of the four components.

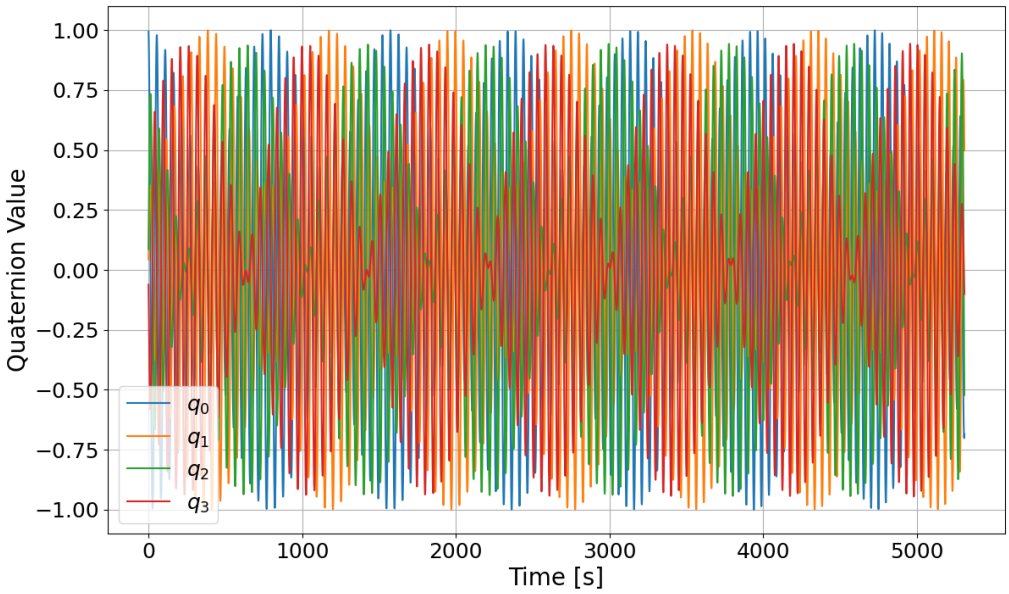

Figure 4.3 Components of the Quaternions $\mathbf{q}$ without Noise and Disturbances (Time Step = 1s).

The quaternion components oscillate periodically over time, which is consistent with the behavior of the rotation matrix $\boldsymbol{A}_{BN}$. This is expected as quaternions provide an alternative but equivalent representation of the spacecraft's attitude. The periodic oscillations of the quaternion components mirror those of the $\boldsymbol{A}_{BN}$ and confirm the stability of the simulation under ideal conditions. This result shows that, also the conversion between the rotation matrix $\boldsymbol{A}_{BN}$ and the quaternions functions flawlessly, confirming the reliability of the attitude representation.

Figure 4.4 shows the magnitude of the angular velocity in the body fixed frame for one orbital period. The magnitude of the angular velocity ω_B increases linearly due to the cross-product term in the provided equation 2.3.

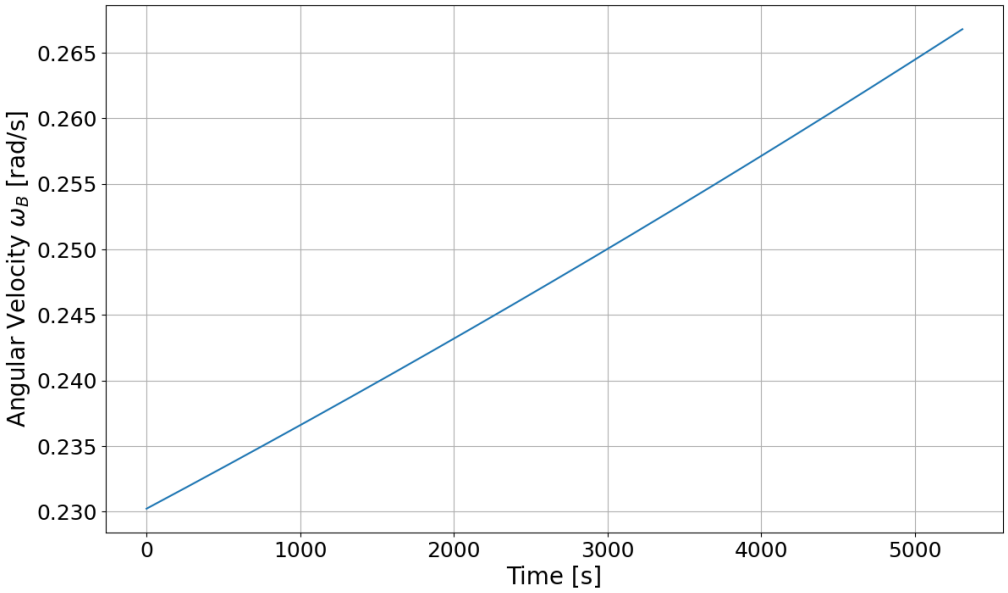

Figure 4.4 Angular Velocity without Noise and Disturbances (Time Step = 1s).

This is expected under ideal conditions without external disturbances in the body fixed frame. However in the inertial frame it should be equal to zero.

Understanding this baseline is critical as it allows to compare how noise and disturbances affect the system. The stability seen here sets the benchmark for evaluating the performance under more realistic conditions.

4.1.2 Disturbances

Here, the effects of the disturbances, described in Chapter 3, on the rotation matrix $\boldsymbol{A}_{BN}$, quaternion $\mathbf{q}$ and angular velocity ω_B is shown. Figure 4.5 shows the effect of the disturbances on the rotation matrix $\boldsymbol{A}_{BN}$ over two orbital periods. For clarity, only the three components of the first row are shown. Compared to the ideal conditions, the rotation matrix components with disturbances exhibit lower peaks, indicating that $\boldsymbol{A}_{BN}$ is slightly affected by the disturbances, introduced in Chapter 3, over two orbital periods.

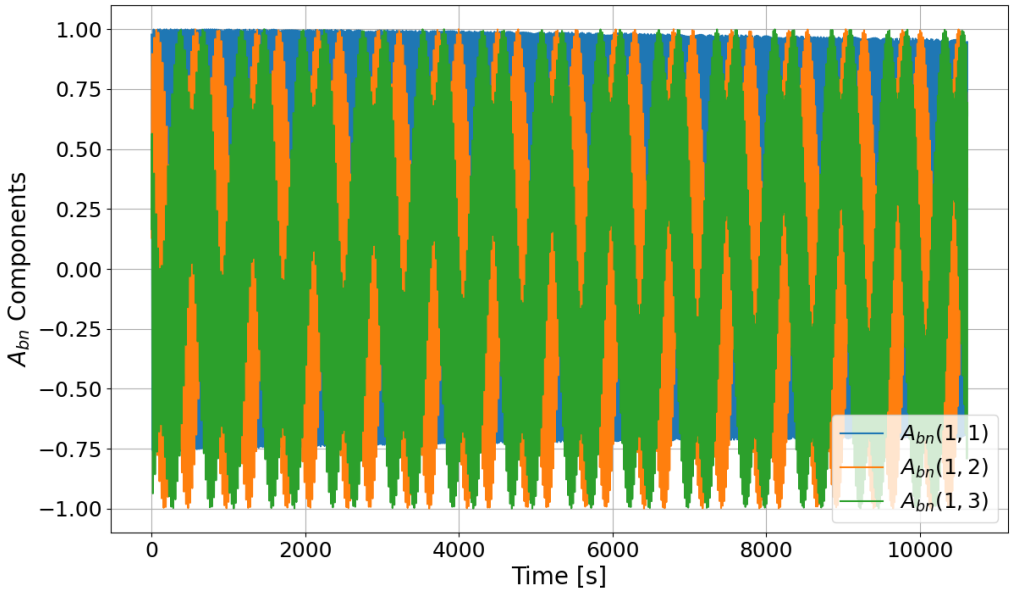

Figure 4.5 Components of the Rotation Matrix $\boldsymbol{A}_{BN}$ with Disturbances (Time Step = 0.1s).

Figure 4.6 shows the behavior of the quaternions $\mathbf{q}$ over two orbital periods. Similar to the $\boldsymbol{A}_{BN}$, the quaternion components also show decreased peak values compared to the ideal scenario. This reflects the impact of disturbances on the quaternions.

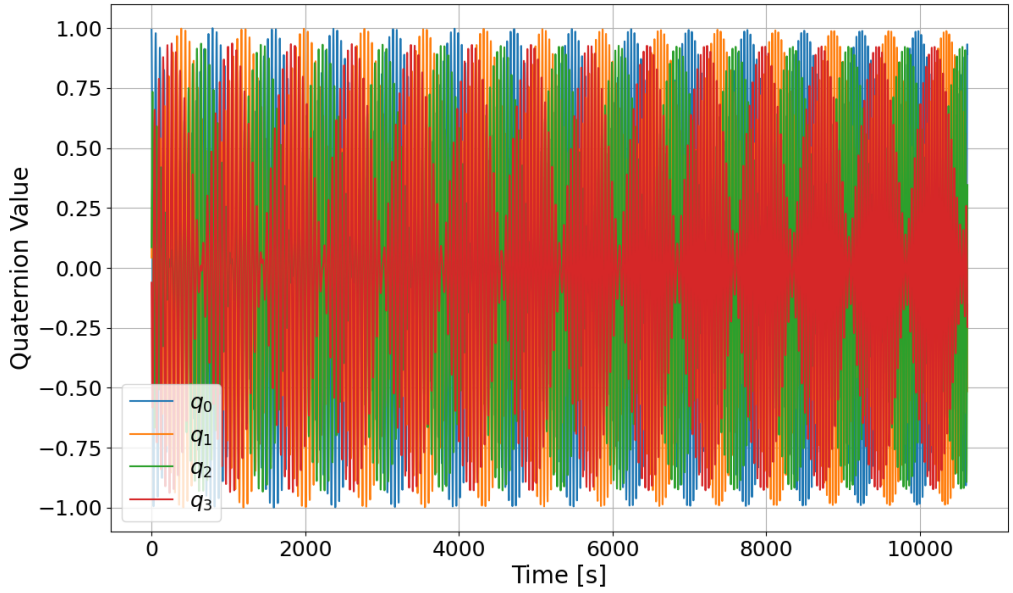

Figure 4.6 Components of the Quaternions $\mathbf{q}$ with Disturbances (Time Step = 1s).

Although the magnitude of the disturbances is relatively low, as mentioned in Section 3.3, their influence on the attitude over two orbital periods is still significant. This influence is visible in the diagrams as small but noticeable changes in the position of the CubeSat. In Figure 4.5, the magnitude of the component of the first row and first column of the rotation matrix $\mathbf{A}_{BN}$ decreases over time. Additionally, the periodicity

becomes smaller due to the satellite's increasing rotation speed. Figure 4.6 underlines this result as the value changes more rapidly.

The disturbances also influence the angular velocity, as shown in Figure 4.7. The magnitude of the angular velocity increases more quickly and reaches a higher value after two orbital periods, as expected, due to the additional rotational effects induced by the disturbances.

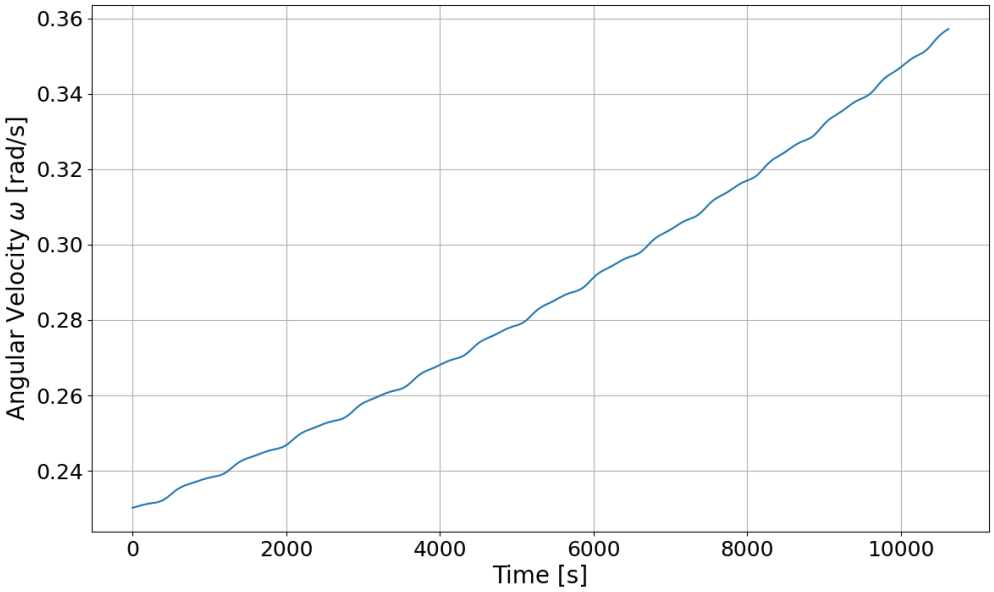

Figure 4.7 Angular Velocity in the Body-Fixed Frame ω_B with Disturbances (Time Step = 1s).

Compared to the ideal conditions, the angular velocity with disturbances increases even more. It is crucial to understand the impact of disturbances for assessing the CubeSat's performance in real-world conditions, where external factors affect its attitude control system.

4.1.3 Noise

In this simulation, the noise was added to the quaternions $\mathbf{q}$, as described in Section 3.4. The effects of the noise on the quaternions can be seen in Figure 4.8.

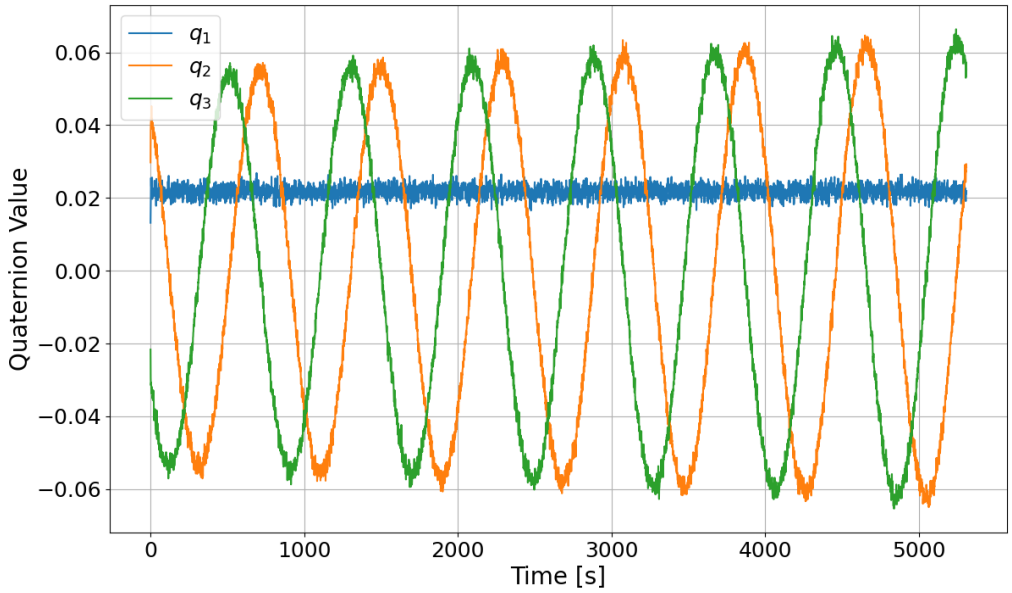

Figure 4.8 Three Components of the Quaternions with Noise (Time Step = 1s).

The addition of noise introduces random variations in the components of $\mathbf{q}$, causing fluctuations not present under ideal conditions. These variations can impact the stability and accuracy of the CubeSat's attitude determination. This naturally affects the rotation matrix $\mathbf{A}_{BN}$ as well, as depicted in Figure 4.9. The rotation matrix components exhibit similar fluctuations due to the noise.

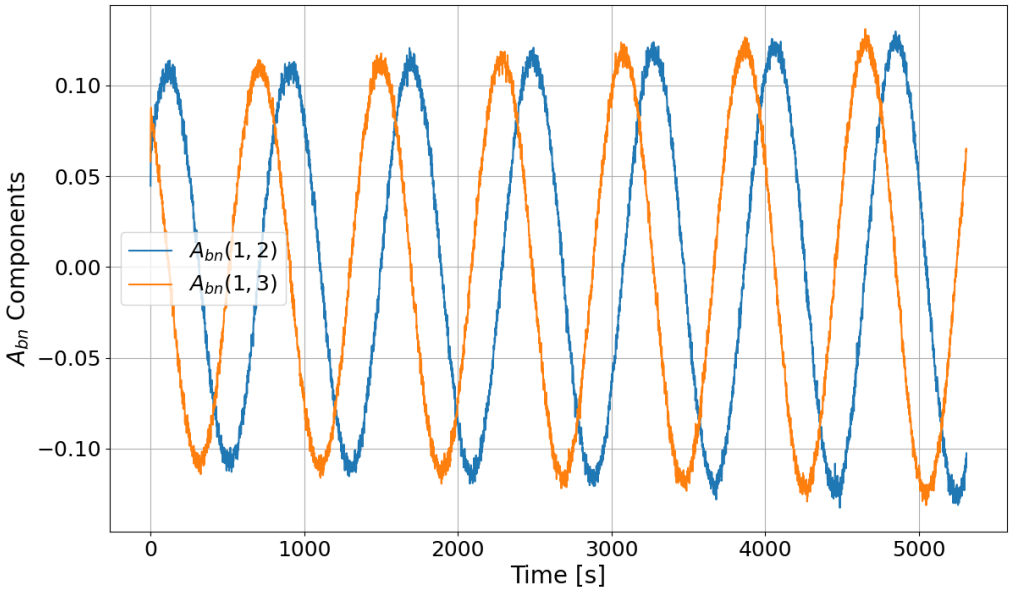

Figure 4.9 Two Components of the Rotation Matrix $\mathbf{A}_{BN}$ with Noise (Time Step = 1s).

The noise affects the rotation matrix by introducing errors into the representation of the attitude, making it less stable compared to the ideal scenarios. This demonstrates the importance of robust filtering and noise reduction techniques to ensure accurate attitude determination under real-world conditions.

The angular velocity is also influenced by the noise, as shown in Figure 4.10 over five seconds. The presence of noise causes the angular velocity to fluctuate, which affects the overall stability of the CubeSat's attitude.

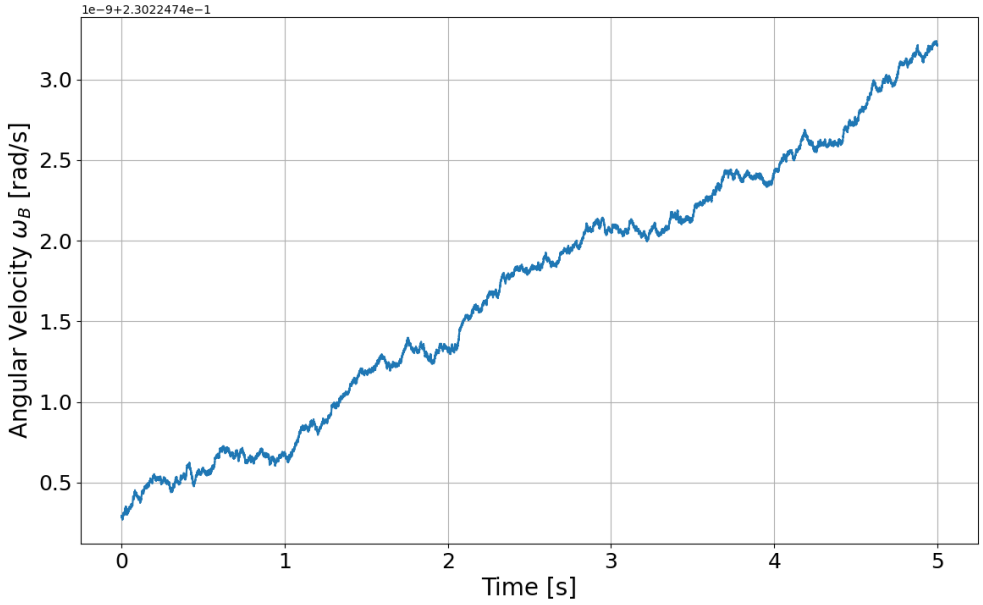

Figure 4.10 Angular Velocity in the Body-Fixed Frame ω_B with Noise (Time Step = 0.0001s).

Considering that the magnitude of the gyroscope noise is about $10^{-12}\frac{rad}{s}$, the impact is not highly visible. Therefore, the data was zoomed in and observed over a period of five seconds in order to better understand the effect. The noises are visible in the fluctuations. The impact of the noise is crucial to real circumstances and to develop a control system capable of acting on both the disturbances and the noise. It should ensure the ADCS remains accurate and stable in the presence of sensor noise.

4.2 Detumbling

In this section, the detumbling maneuver is tested and analyzed under different scenarios to evaluate the effectiveness of various actuators. In this case, the noise was added to the rotation matrix $\mathbf{A}_{BN}$. The following actuator configurations are considered:

- Three magnetorquers without reaction wheels
- Three reaction wheels
- Three magnetorquers with two reaction wheels

Scenario 1: Three Magnetorquers

In the first scenario, the detumbling maneuver uses only three magnetorquers. Figure 4.11 shows the time evolution of the angular velocity components $\boldsymbol{\omega}_B = [\omega_x, \omega_y, \omega_z]^T$ during this maneuver over two orbital periods. The plot shows that the angular velocity components reach zero after approximately $6000s$, which equals the settling time. The angular velocity components still oscillate around zero after settling time.

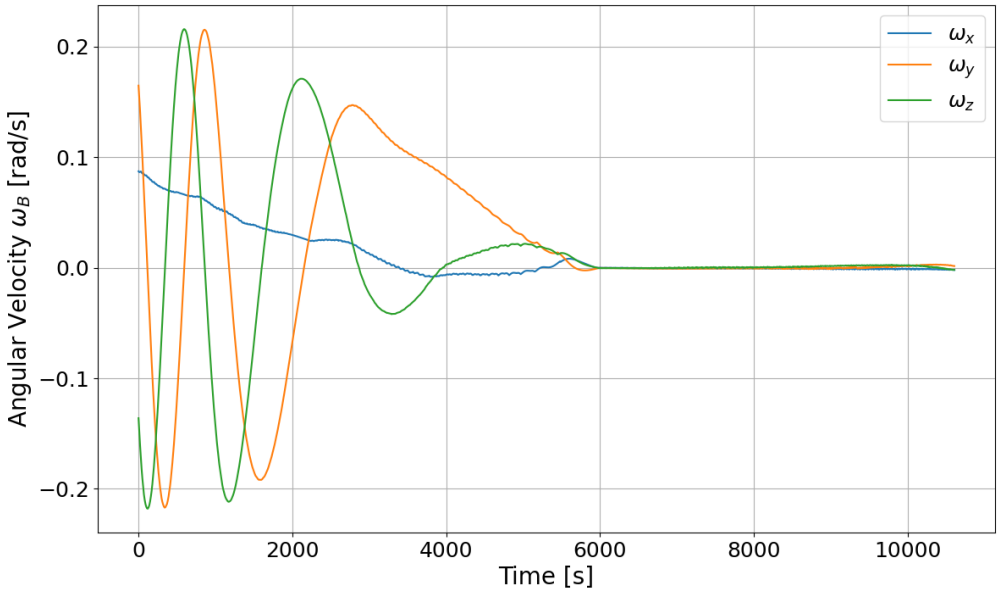

Figure 4.11 Angular Velocity Components during Detumbling using Three Magnetorquers (Time Step = 1s).

The angular velocity components decrease over time, indicating that the magnetorquers are effectively reducing the rotation rates of the CubeSat. However, the detumbling process is relatively slow due to the limited control torque of the magnetorquers alone. Furthermore the oscillations around zero are still visible in the plot.

Additionally, Figure 4.12 shows the evolution of the quaternion components $\mathbf{q} = [q_0, q_1, q_2, q_3]^T$ during the detumbling maneuver.

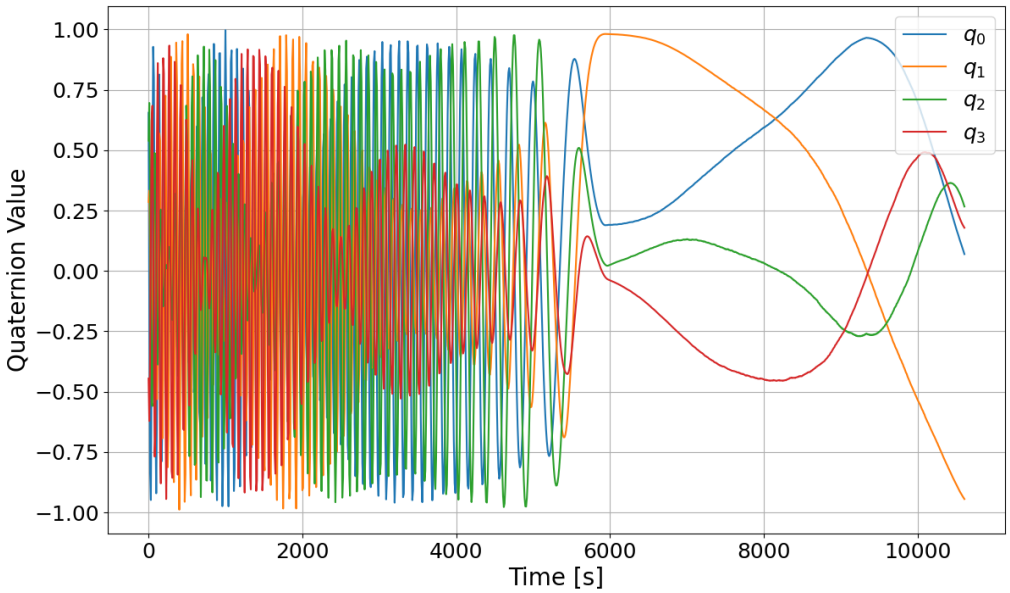

Figure 4.12 Quaternion Components during Detumbling using Three Magnetorquers (Time Step = 1s).

The quaternion components also show a gradual stabilization over time, indicating that the CubeSat's orientation is becoming more controlled as the detumbling progresses. However, the oscillations in the

quaternion components suggest that the magnetorquers alone do not provide enough control for rapid stabilization, resulting in slower convergence to the desired attitude.

Figure 4.13 shows the components of the control torque $\mathbf{u} = [u_x, u_y, u_z]^T$ of the magnetorquers over the time. The magnitude of the control torque is about $10^{-6} Nm$. The plot clearly shows the activation period of each magnetorquer, indicating that they must remain active to maintain a velocity close to zero.

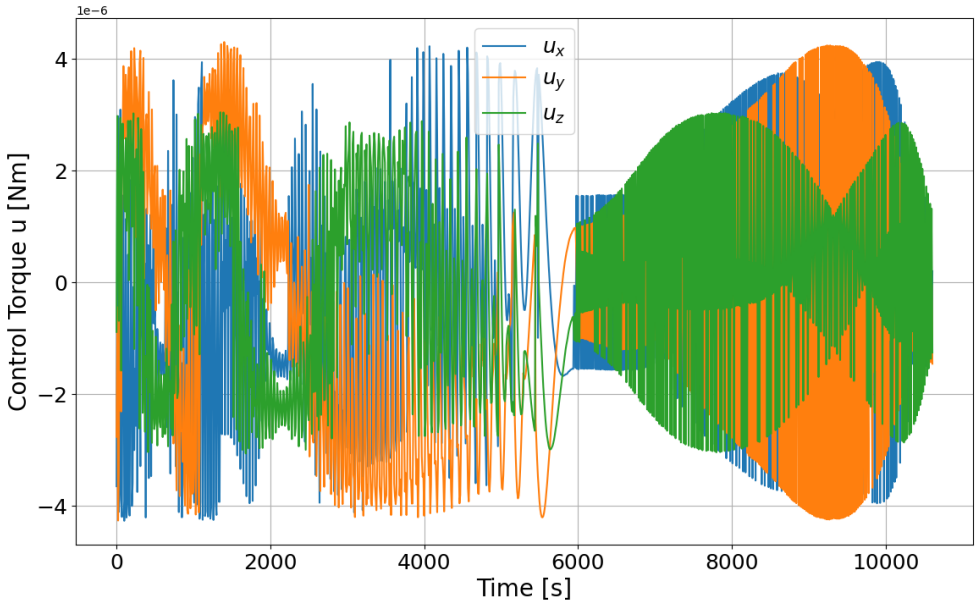

Figure 4.13 Control Torque during Detumbling using Three Magnetorquers (Time Step = 1s).

Scenario 2: Three Reaction Wheels

In the second scenario, three reaction wheels were utilized to provide the required control torque. The analysis involves observing the evolution of the angular velocity components, the quaternion components and the control torque during the detumbling over two orbital periods with a time step of $\Delta t = 1s$.

Figure 4.14 shows the angular velocity components during this maneuver.

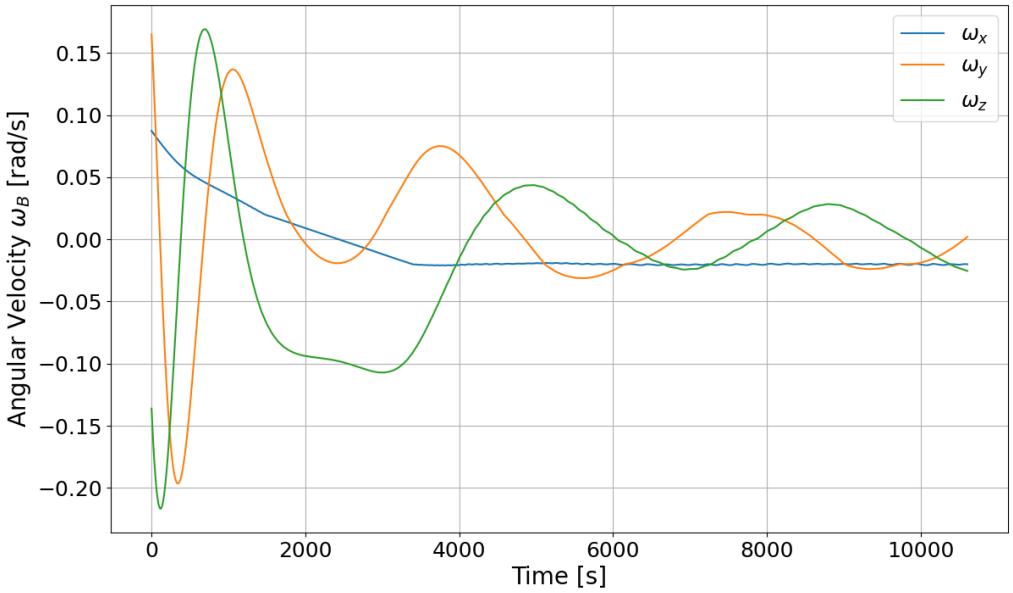

Figure 4.14 Angular Velocity during Detumbling using Three Reaction Wheels (Time Step = 1s).

The plot indicates that the angular velocity components take a longer time to reach zero with significant oscillations throughout the maneuver. The settling time is not clearly defined due to these persistent oscillations. However, after $6000s$, the angular velocity components oscillate within the threshold. The threshold in this scenario was set to $\omega_{threshold} = 0.02\frac{rad}{s}$ to get closer to zero. This suggests that the reaction wheels, in this case, introduce more instability into the system, resulting in prolonged oscillations around zero.

In Figure 4.15 the quaternion components of the satellite are shown.

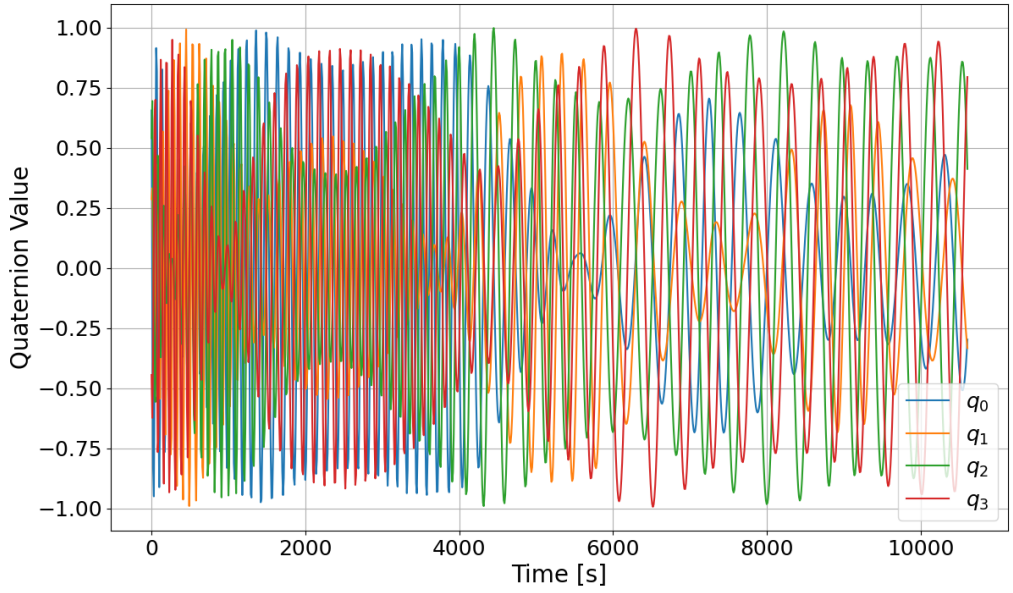

Figure 4.15 Quaternion Components during Detumbling using Three Reaction Wheels (Time Step = 1s).

The quaternion components exhibit significant oscillations throughout the maneuver, indicating that the attitude of the CubeSat is constantly changing due to the oscillations in angular velocity. This constant change in attitude reflects the instability created by the reaction wheels in this scenario.

Figure 4.16 depicts the control torque components of the reaction wheels.

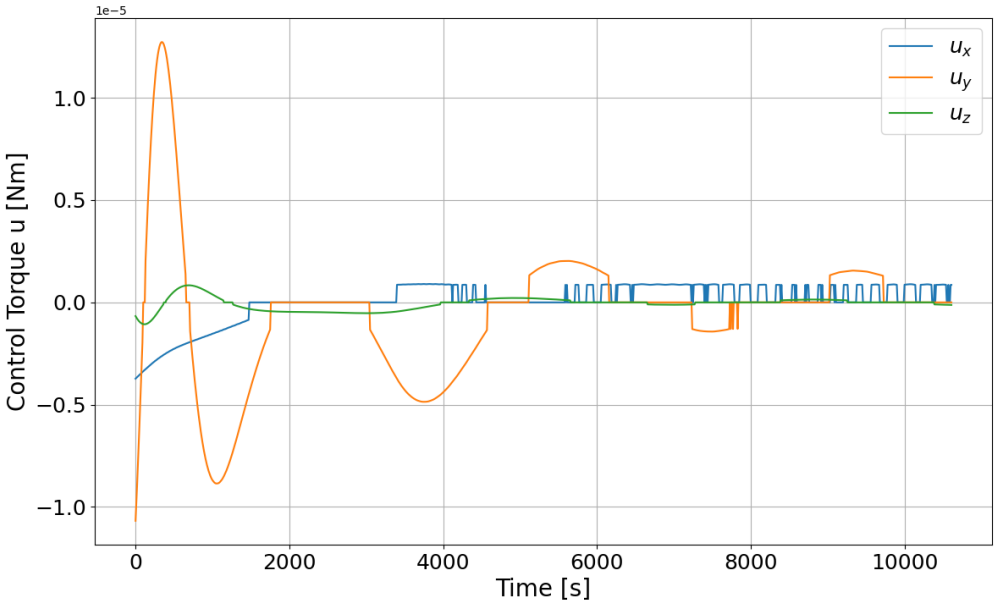

Figure 4.16 Control Torque during Detumbling using Three Reaction Wheels (Time Step = 1s).

The peaks show the activation of the actuators and that the reaction wheels are not always active. However, after approximately $5000s$, the x-component of the control torque needs to be activated almost constantly to maintain the angular velocity within the threshold. This continuous adjustment contributes to the observed oscillations of the angular velocity and quaternion components.

Scenario 3: Magnetorquers with Two Reaction Wheels

In the third scenario, two reaction wheels are used with the three magnetorquers. For the threshold angular velocity $\omega_{threshold}$, the value $0.05\frac{rad}{s}$ showed the best results for detumbling. Figure 4.17 shows the angular velocity components during the detumbling with this actuator configuration over two orbital periods. The angular velocity reaches zero after approximately $3000s$. This is significantly faster and more stable compared to the scenarios with only three magnetorquer and only three reaction wheels. The detumbling with this configuration only requires 50% of the time needed by the other maneuvers.

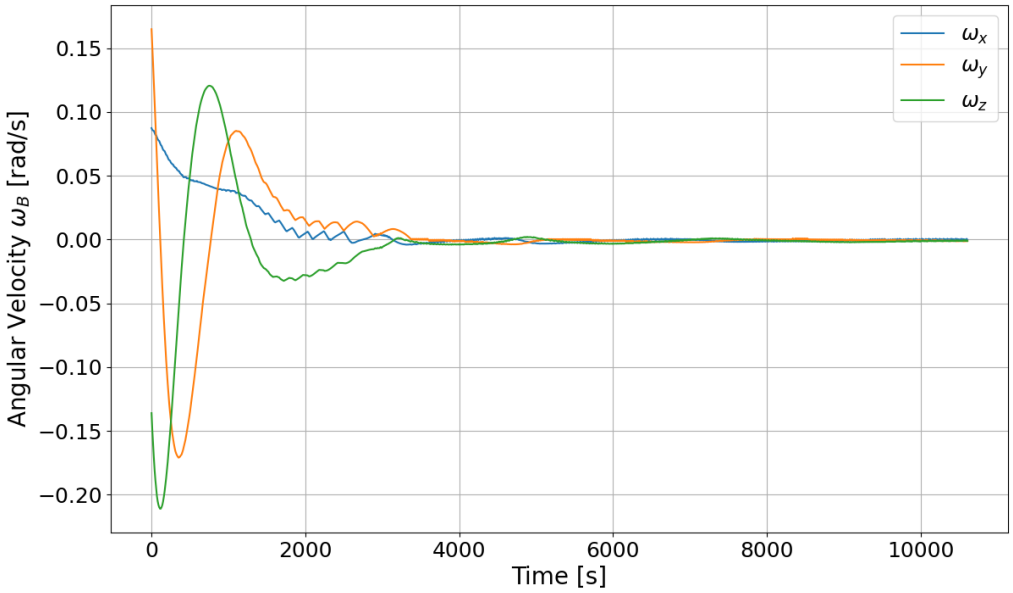

Figure 4.17 Detumbling using Three Magnetorquers with Two Reaction Wheels (Time Step = 1s).

Figure 4.18 shows the components of the quaternions during the detumbling in this configuration. Just as the angular velocity reaches zero faster, the quaternions also saturate faster, as the control torque provided by the reaction wheels is stronger.

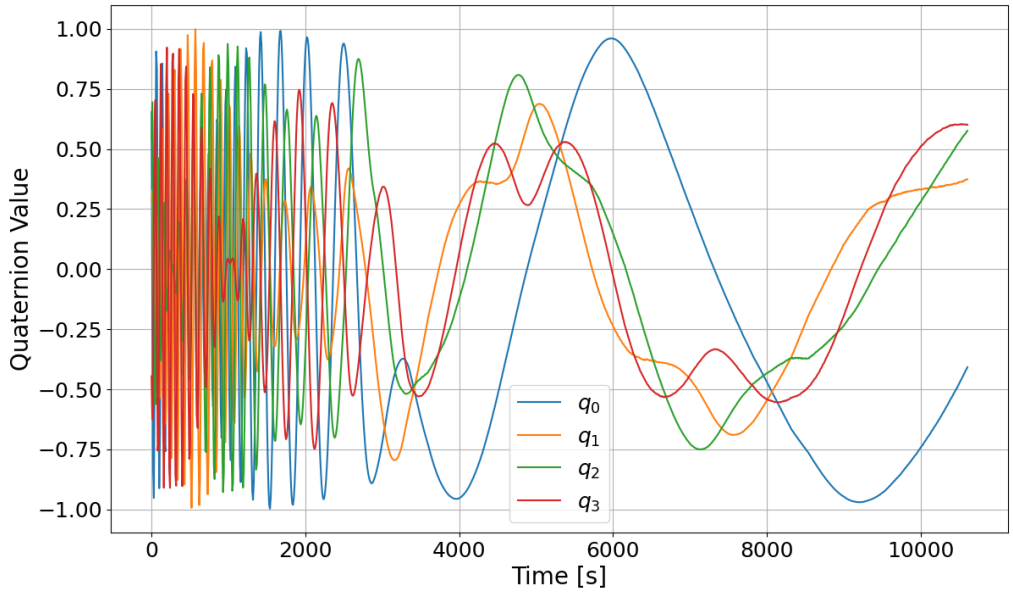

Figure 4.18 Quaternion Components during Detumbling using Three Magnetorquers and Two Reaction Wheels (Time Step = 1s).

The actuators' control torque components are depicted in Figure 4.19.

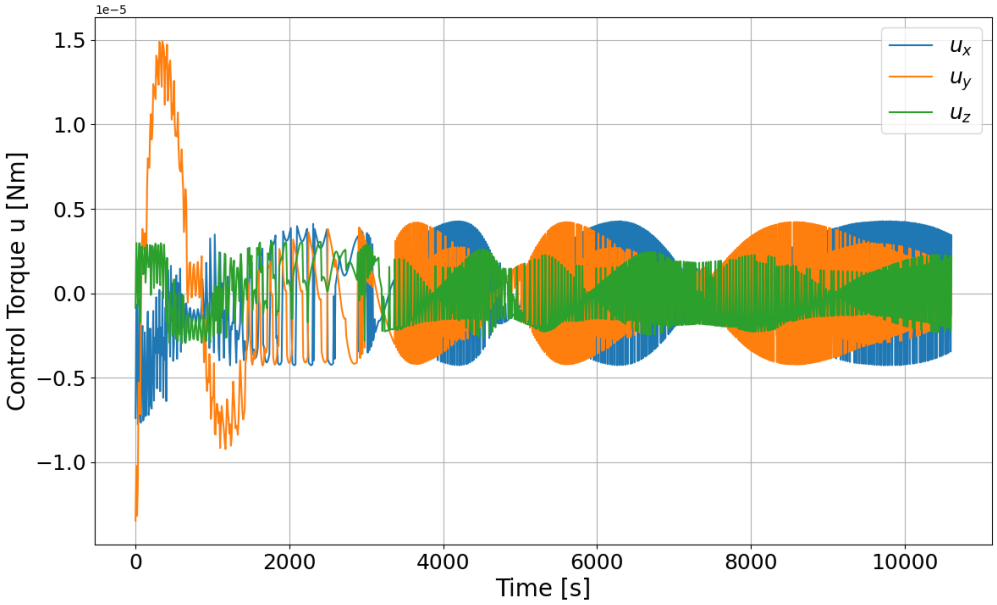

Figure 4.19 Control Torque during Detumbling using Three Magnetorquers and Two Reaction Wheels (Time Step = 1s).

Here, the control torque shows a few spikes, as seen at approximately $500s$, where u_y peaks, as the reaction wheel, generating torque for the y-axis, was activated. This configuration provides the faster detumbling performance. The angular velocity components decrease rapidly, demonstrating the effectiveness of combining magnetorquers with the reaction wheels. The reaction wheel produces additional control torque, which allows a faster reduction of the CubeSat's angular velocity.

Comparison of Scenarios

When comparing the three scenarios, it is evident that adding reaction wheels to magnetorquer significantly improves the detumbling performance. The angular velocity decreases most rapidly when two reaction wheels are used in addition to the magnetorquers. This actuator configuration reduces the settling time by 50%. Using only magnetorquers is still stable, however the detumbling requires in this configuration $6000s$. In contrast to this, employing only reaction wheels leads to more instability and oscillations with the same settling time as for only magnetorquers. This is why combining three magnetorquer with two reaction wheels is the most effective. This emphasizes the importance of an ADCS with sufficient control capability to achieve fast and efficient detumbling.

4.3 Pointing Results

In this section, the pointing maneuver is tested using three reaction wheels. The objective of the pointing maneuver is to orient the CubeSat towards the meteoroid, which is analyzed through the angle $\boldsymbol{\theta}$, as explained in Section 3.6.2. Ideally, all components of $\boldsymbol{\theta}$ should approach to zero, indicating accurate pointing. For this maneuver the initial angular velocity was set to

$$\boldsymbol{\omega} = [0, 0, 0]^T \quad \frac{rad}{s} \tag{4.2}$$

Figure 4.20 shows the evolution of the angle $\boldsymbol{\theta}$ over time during the pointing maneuver. For the simulation a time step of $\Delta t = 1s$, was used and one orbital period was analyzed.

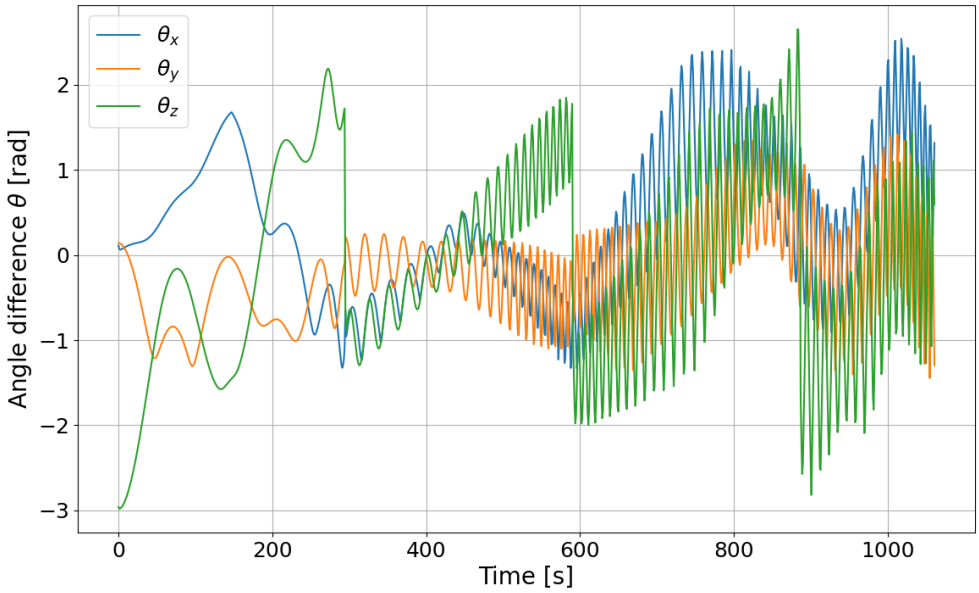

Figure 4.20 Angle θ during Pointing Maneuver using Reaction Wheels (Time Step = 1s).

The plot indicates that the pointing is achieved at around $400s$, as the components of θ reach zero at this point. However, this state is subsequently lost and the pointing cannot be maintained by the control. This incomplete convergence suggests that the proportional system is not sufficient. For precise pointing, a more complex control logic is required. The residual angle $\boldsymbol{\theta}$ indicates that the control effort is inadequate to overcome disturbances and achieve the desired attitude.

This result underscores the need to enhance the control system by improving the control algorithms to ensure more effective pointing.

Additionally, the angular velocity components during the pointing maneuver are shown in Figure 4.21, highlighting the dynamic response of the reaction wheels.

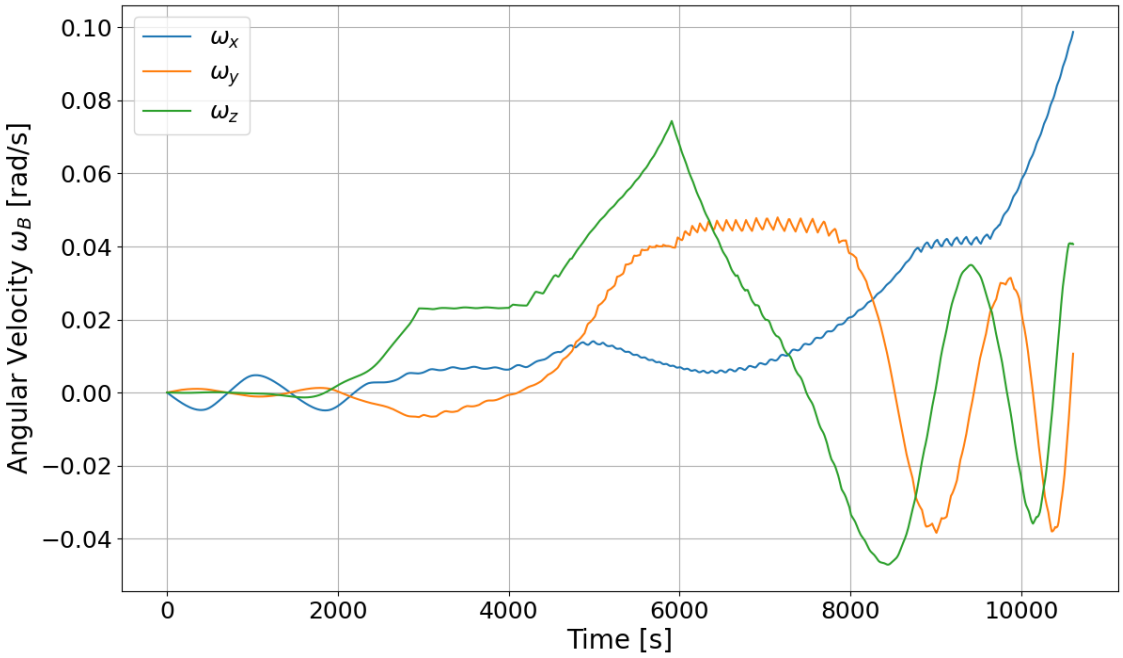

Figure 4.21 Angular Velocity Components during Pointing Maneuver using Three Reaction Wheels (Time Step = 1s).

The angular velocity components indicate the efforts made by the reaction wheels to adjust the CubeSat's orientation. However, the persistent non-zero θ demonstrates that these efforts are insufficient under the current control configuration.

Understanding these limitations is crucial for developing more robust pointing strategies. Future work could enhance the reaction wheel control system or integrate additional control elements to achieve the desired pointing accuracy.

5 Conclusion and Outlook

5.1 Conclusions

In this thesis, the ADCS for a 6U CubeSat was developed and analyzed using Python. The subsystem was focused on detumbling of the satellite and pointing at a meteoroid. The results show the effectiveness of different actuator configurations and control laws.

For the detumbling, combining three magnetorquers and two reaction wheels provided superior performance compared to using magnetorquers alone. The additional reaction wheels produced a higher control torque, resulting in a faster reduction in angular velocity and the ability to align it to zero more efficiently. Specifically, this configuration reduced the settling time by 50%, with the detumbling taking approximately 3000 seconds compared to 6000 seconds using magnetorquers or reaction wheels alone. This demonstrates that the use of reaction wheels in addition to magnetorquers significantly enhances the detumbling process. Furthermore, the proportional control law was proved adequate for the detumbling maneuver, and sufficient stabilization was achieved without needing more complex control strategies. Table 5.1 summarizes the different results of the scenarios.

Configuration	Settling Time (seconds)	Notes
Three Magnetorquers	6000	Stable, slow detumbling
Three Reaction Wheels	6000	Instability and oscillations
Three Magnetorquers + Two Reaction Wheels	3000	Fast and efficient detumbling

Table 5.1 Detumbling Performance Comparison

In contrast, the pointing maneuver faced more challenges. The same proportional control law used for the detumbling was insufficient for accurately pointing at a target. The control was unable to overcome the disturbances and align with the target. Therefore an angle between the target and the satellite's pointing direction remained throughout the control. This limitation may require a more complex control strategy to achieve precise pointing.

To summarize, the proportional control law is effective for detumbling maneuvers. However, it is not sufficient to achieve precise pointing accuracy.

5.2 Future Work

Future work should focus on developing and implementing advanced control methods to achieve precise pointing accuracy. Examples include proportional-integral-derivative (PID) control or adaptive control techniques. The control could expand tracking and following the meteoroid. Moreover, the ADCS could be adapted for various mission-specific applications, such as Earth observation, telecommunications and interplanetary missions. Each application has unique requirements and challenges that could drive the development of specialized control algorithms. Exploring the application of ADCS to different sizes and types of satellites could also be beneficial. For example, adapting control strategies for larger satellites or constellations of small satellites could require approaches tailored to account for different dynamics and control requirements. Additionally, the ADCS could be interfaced with real hardware for Hardware-In-The-Loop (HIL)-testing, further validation, and refining the control strategies.

Bibliography

[1] Meteoroid environment office. https://www.nasa.gov/meteoroid-environment-office/. Accessed: 2024-06-21.

[2] State-of-the-art small spacecraft technology: Chapter 5.0 guidance, navigation, and control. Technical Report NASA/TP—2024–0001462, Small Spacecraft Systems Virtual Institute, NASA Ames Research Center, Moffett Field, CA, 2024. Available at https://ntrs.nasa.gov/citations/20110007876.

[3] V. A. Bronshten. *Physics of Meteoric Phenomena*. Geophysics and Astrophysics Monographs. D. Reidel Publishing Company, Dordrecht, Holland, 1983.

[4] E. Buchen. Small satellite market observations. In *Proceedings of the Small Satellite Conference*, 2015. Session VII, Paper SSC15-VII-7.

[5] L. Cao, W. Yang, H. Li, Z. Zhang, and J. Shi. Robust double gain unscented kalman filter for small satellite attitude estimation. *Advances in Space Research*, 60(3):499–512, 2017.

[6] CubeSat Design Specification Rev. 14.1. Cubesat design specification rev. 14.1. Technical report, The CubeSat Program, Cal Poly SLO, San Luis Obispo, CA, 2022.

[7] CubeSpace. Adcs actuators. https://www.cubespace.co.za/products/#actuators. Accessed: 2024-06-25.

[8] K. Gaber, M. B. El_Mashade, and G. A. A. Aziz. Real-time implementation of a robust simplified intelligent proportional–integral control for cubesat attitude determination system. *Control Engineering Practice*, 98:104377, 2020.

[9] A. Hanslmeier. *The Sun and Space Weather*, volume 277 of *Astrophysics and Space Science Library*. Kluwer Academic Publishers, Dordrecht, 2002.

[10] F. Holzapfel. Introduction to flight mechanics, 2023. Lecture notes, Technical University of Munich.

[11] G. Juchnikowski, T. Barciński, and J. Lisowski. Optimal control gain for satellite detumbling using b-dot algorithm. 2013.

[12] S. A. Khan, Y. Shiyou, A. Ali, M. Tahir, S. Fahad, S. Rao, and M. Waseem. Pcb-integrated embedded planar magnetorquers for small satellites intelligent detumbling. *Computers and Electrical Engineering*, 108, 2023.

[13] D. Koschny, R. H. Soja, C. Engrand, G. J. Flynn, J. Lasue, A.-C. Levasseur-Regourd, D. Malaspina, T. Nakamura, A. R. Poppe, V. J. Sterken, and J. M. Trigo-Rodríguez. Interplanetary dust, meteoroids, meteors and meteorites. *Space Science Reviews*, 215(4):34, 2019.

[14] W. J. Larson and J. R. Wertz, editors. *Space Mission Analysis and Design*. Space Technology Library. Microcosm Press and Kluwer Academic Publishers, El Segundo, California and Dordrecht / Boston / London, 3rd edition, 1999. Seventh printing, 2005.

[15] N. Liu, K. Hung, B. Lyu, S. Yang, Y. Lin, and C. Yu Chan. Reaction wheel design for precise attitude control of cubesats using flexible pcb windings and halbach magnet array. *IEEE Transactions on Aerospace and Electronic Systems*, pages 1–13, 2024.

[16] M. Marin and H. Bang. Design and simulation of a high-speed star tracker for direct optical feedback control in adcs. *Sensors (Switzerland)*, 20(8), 2020.

[17] V. Messina. Detumbling & sun pointing of a 3u cubesat, 2021.

[18] V. Messina. Basic satellites propagation. https://gitlab.lrz.de/VinMes/basicsatellitespropagation, 2024. Accessed: 2024-07-02.

[19] M. Paluszek. Chapter 4 - acs system design. In *ADCS - Spacecraft Attitude Determination and Control*, pages 33–45. Elsevier, 2023.

[20] A. Poghosyan and A. Golkar. Cubesat evolution: Analyzing cubesat capabilities for conducting science missions. *Progress in Aerospace Sciences*, 88:59–83, 2017.

[21] A. Porras-Hermoso, J. González-Monge, S. Marín-Coca, and E. Roibás-Millán. Optimal sun-tracking law for remote sensing satellites operating under observation constraints. *Acta Astronautica*, 222:95–108, 2024.

[22] E. Rieger. Adcs for a 6u cubesat for tracking objects in space. https://gitlab.lrz.de/00000000014A9B99/adcs.git, 2024. Accessed: 2024-07-02.

[23] D. Rose. Rotation quaternions and how to use them, 2015. Accessed: 2024-06-24.

[24] D. Selva and D. Krejci. A survey and assessment of the capabilities of cubesats for earth observation. *Acta Astronautica*, 74:50–68, 2012.

[25] R. Starin. and J. Eterno. Attitude determination and control systems. Technical Report 20110007876, NASA Goddard Space Flight Center, Southwest Research Institute, 2011. Available at https://ntrs.nasa.gov/citations/20110007876.

[26] NASA Science Editorial Team. 10 things: Cubesats — going farther. https://science.nasa.gov/solar-system/10-things-cubesats-going-farther/, 2019. Accessed: 2024-05-31.

[27] D. Vida, J. M. Scott, J. Vaubaillon A. Egal, Q.-Z. Ye, D. Rollinson, M. Sato, and D. E. Moser. Observations of the new meteor shower from comet 46p/wirtanen. *Astronomy & Astrophysics*, 682, 2024.

[28] R. Walker. Technology cubesats. https://www.esa.int/Enabling_Support/Space_Engineering_Technology/Technology_CubeSats. Accessed: 2024-05-31.

[29] J. R. Wertz., editor. *Spacecraft Attitude Determination and Control*. Kluwer Academic Publishers, Dordrecht, Boston, London, 1978. Preparation of this material was supported by the Attitude Determination and Control Section, Goddard Space Flight Center, National Aeronautics and Space Administration under Contract No. NAS 5-11999 and by the System Sciences Division, Computer Sciences Corporation.

[30] X. Zhang, Y. Geng, and B. Wu. Approaching and pointing tracking control for tumbling target under motion constraints. *Acta Astronautica*, 209:6–20, 2023.